Inertial motion on the Earth's spheroidal surface

Boyd F. Edwards (corresponding author: boyd.edwards@usu.edu) and Cade Pankey
Department of Physics
Utah State University, Logan, Utah 84322

John M. Edwards
Department of Computer Science
Utah State University, Logan, Utah 84322
(Dated: November 29, 2022)

As seen by an observer in the rotating frame, the earth's small spheroidal deformations neutralize the centrifugal force, leaving only the smaller Coriolis force to govern the "inertial" motion of objects that move on its surface, assumed smooth and frictionless. Previous studies of inertial motion employ weakly spheroidal equations of motion that ignore the influence of the centrifugal force and yet treat the earth as a sphere. The latitude dependence of these equations renders them strongly nonlinear. We derive and justify these equations and use them to identify, classify, name, describe, and illustrate all possible classes of inertial motion, including a new class of motion called circumpolar waves, which encircle both poles during each cycle of the motion. We illustrate these classes using *CorioVis*, our freely available Coriolis visualization software. We identify a rotational/time-reversal symmetry for motion on the earth's surface and use this symmetry to develop and validate closed-form small-amplitude approximations for the four main classes and one degenerate class of inertial motion. For these five classes, we supply calculations of experimentally relevant frequencies, zonal drifts, and latitude ranges.

The nonlinear dynamics of an object that moves over large distances on the earth's surface is fundamental to meteorology, oceanography, aviation, and ballistics. This motion is complicated by the earth's equatorial bulge, the inertial forces experienced by an earthbound observer in the frame of the rotating earth, and the nonlinear dependence of these forces on latitude. There are four main classes of such motion, three of which have been described previously. We use symmetry arguments and visualizations to identify and describe all four main classes and twelve degenerate classes. The new main class, called circumpolar waves, encircles both poles during each cycle of the motion. The degenerate classes cross one or both poles, approach the equator asymptotically, or remain at a fixed latitude. We show that these sixteen classes completely characterize the motion of an object on the earth's spheroidal surface, assumed smooth and frictionless.

I. INTRODUCTION

The Coriolis force plays important roles in meteorology [1], oceanography [2], ballistics [3], sniping [4], aviation [5], space stations [6], and playgrounds [7], and has a long history of study. In 1679, Sir Isaac Newton and Robert Hooke discussed the possibility that the horizontal deflection of falling objects could serve as proof of the Earth's rotation; this possibility was confirmed in an 1803 measurement that agreed with calculations by Gauss and Laplace [8]. In 1835, Gaspard Gustave Coriolis showed that the total inertial force on an object as seen by an observer in a rotating frame is the sum of two forces, the centrifugal force and a "deflective force" that is now known as the Coriolis force [8–10]. The Coriolis force applies only when the object moves relative to this frame, whereas the centrifugal force applies with or without such motion [11, 12].

As seen by an observer in the inertial frame, a puck sliding on the surface of a frictionless rotating sphere experiences opposing but unbalanced gravitational and normal forces, and executes uniform circular motion in great circles. As seen by an observer in the rotating frame, the puck also experiences the Coriolis and centrifugal forces, which complicate the motion in this frame [13]. For motion on a sphere, the speed of the puck and its axial angular momentum are conserved in the inertial frame.

The earth's small spheroidal deformations play an outsized role in motion on its spheroidal surface, assumed smooth and frictionless. These deformations neutralize the centrifugal force, leaving only the smaller Coriolis force to govern the motion, as seen by observers in the rotating frame [14, 15]. Because the Coriolis force is perpendicular to the puck velocity, the puck speed is conserved in the rotating frame, while its axial angular momentum is conserved in the inertial frame [16]. Consequently, "inertial" motion on the spheroidal earth differs profoundly from motion on a sphere.

Theoretical investigations of inertial motion are based on a weakly spheroidal approximation that ignores the influence of the centrifugal force and yet treats the earth as a sphere [17–28]. This approximation seems paradoxical because it is the earth's spheroidal deformations that are responsible for neutralizing the centrifugal force.

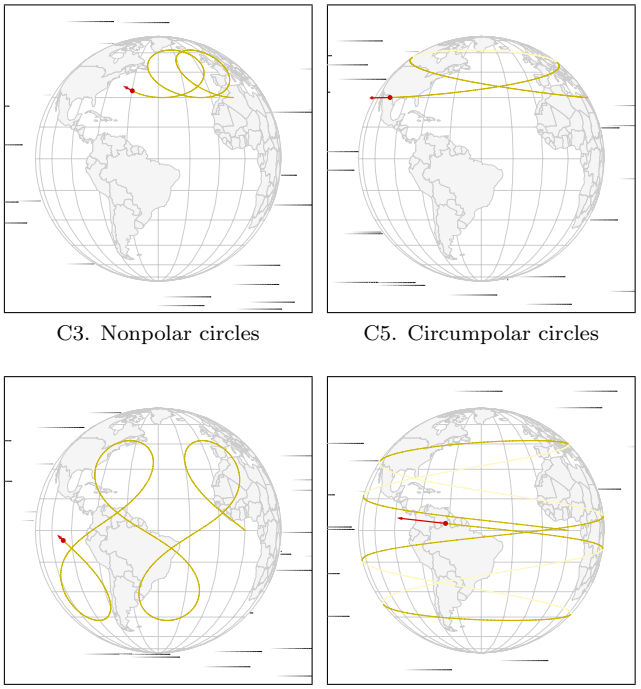

C3. Nonpolar circles C5. Circumpolar circles

C13. Nonpolar waves C15. Circumpolar waves

FIG. 1. Screenshots of *CorioVis* visualizations of the four main classes of inertial motion of a puck that slides on the earth's stably rotating spheroidal surface, assumed frictionless, as seen by an observer in the rotating frame, labeled by their *CorioVis* demonstration numbers [32]. Puck trajectories are shown in yellow. Red dots denote final puck positions and red arrows denote final puck velocities.

In this paper, we derive and justify the weakly spheroidal approximation by applying exact equations of motion for an object moving on the surface of a stably rotating uniform spheroid of arbitrary eccentricity [28] to the reference spheroid that is used in terrestrial cartography, geodesy, satellite navigation, and the global positioning system (GPS) [29–31]. On the reference spheroid, the weakly spheroidal approximation agrees with exact solutions to within 1%. We assume throughout that puck velocities are horizontal, tangent to the earth's surface, and that the puck remains in frictionless contact with this surface at all times. The latitude dependence of the weakly spheroidal equations of motion renders these equations strongly nonlinear.

The purpose of this paper is to use the weakly spheroidal equations to identify, classify, name, describe, and illustrate all of the classes of inertial motion on the earth's spheroidal surface, as seen by an observer in the rotating frame. We show that there are four topologically distinct main classes. For all four classes, the puck oscillates between two fixed latitudes and generally drifts either west or east; "nonpolar circles" do not cross the equator or encircle a pole; "circumpolar circles" do not cross the equator but do encircle a pole; "nonpolar waves" cross the equator and do not encircle any poles; and "circumpolar waves" cross the equator and encircle both poles (Fig. 1). The essential topological difference between circumpolar and nonpolar motion is that the zonal velocity component for circumpolar motion is always toward the west.

Three of these four classes have been described previously. Nonpolar circles are often referred to as "inertial circles" [19, Fig. 2], and are the only class to have been observed in ocean and atmospheric currents [8, 33–39]. Circumpolar circles have been described as "westward motion, oscillating in latitude" [22, Fig. 2b]. Nonpolar waves are sometimes referred to as "inertial oscillations" [19, Fig. 2]. Cushman-Roisin describes just two main classes of inertial motion, conflating nonpolar and circumpolar circles into "mid-latitude oscillation and drift in a zonal band" and conflating nonpolar and circumpolar waves into "oscillation and drift in an equatorial zonal band" [17, Table I]. We find no descriptions of circumpolar waves in the literature.

In addition to the four main classes, we study eight degenerate classes and four doubly degenerate classes that are described, in words, by Cushman-Roisin [17, Table I]. Although these degenerate classes are needed for topological completeness and might be observable with carefully chosen initial conditions, random initial conditions and naturally occurring motion will always fall into one of the four main classes.

Trajectories of seven of the sixteen classes of inertial motion have been illustrated previously. Paldor and associates use Cartesian plots of latitude vs. longitude to illustrate six classes [22–25]. They also use polar plots of colatitude (radius) and longitude (azimuthal angle) to further illustrate three of these six classes. Such Cartesian and polar plots distort the trajectories because these plots do not account, respectively, for converging longitude lines toward the poles and parallel longitude lines at the equator. Similarly, Wiin-Nielsen uses Cartesian plots to illustrate two classes and uses polar plots to illustrate four [40]. Cushman-Roisin and Whipple use Cartesian plots to illustrate the same three classes [17, 26]. Ripa and Early use screenshots of trajectories on the earth's surface to illustrate two classes and three classes, respectively [18, 19]. Missing in all these illustrations are one main class (circumpolar waves), five degenerate classes, and three doubly-degenerate classes.

We illustrate all sixteen classes of inertial motion with sixteen *CorioVis* demonstrations that show the motion of the puck on the reference spheroid from any viewing angle and in any of three reference frames (rotating frame, inertial frame, and counter-rotating frame). We use screenshots of these sixteen demonstrations as the basis for our classification scheme and to illustrate time-reversal symmetries. Our illustrations convey immediate understanding of class topologies that is lacking in the word descriptions of Cushman-Roisin [17, Table I]. *CorioVis* is our robust freely available web-based Coriolis visualization software that animates the motion of a puck on the surface of a planet of arbitrary spheroidal eccen-

tricity and of arbitrary angular velocity of rotation, for arbitrary initial puck positions and velocities [32].

Our classification scheme, our descriptive class names, and our visualizations establish the uniqueness of each class and clarify the relationships between classes, including time-reversal symmetries on the counter-rotating earth.

We derive and validate closed-form small-amplitude mathematical descriptions for the four main classes and for one degenerate class, "polar circles," which pass directly over a pole but do not cross the equator. These descriptions supply experimentally relevant analytical expressions for the frequencies, zonal drifts, and latitude ranges of inertial motion that agree with our exact numerical calculations of these quantities in the small-amplitude limit. Small-amplitude nonpolar, polar, and circumpolar circles have frequencies that are independent of the amplitude, whereas small-amplitude nonpolar and circumpolar waves have frequencies that are proportional to the square root of the amplitude. This is because nonpolar and circumpolar waves oscillate about the equator, where the horizontal components of the Coriolis force vanish.

Our small-amplitude descriptions of nonpolar circles and waves apply for small puck speeds as seen by an earthbound observer in the "rotating" frame of a normally rotating earth that rotates toward the east. Our small-amplitude descriptions of circumpolar circles and waves apply for small puck speeds as seen by an earthbound observer in the "counter-rotating" frame of a counter-rotating earth that rotates toward the west. We show that circumpolar circles and waves in the rotating frame become nonpolar circles and waves when viewed in the counter-rotating frame, and show that this rotational symmetry is equivalent to a time-reversal symmetry. Our small-amplitude descriptions are written in terms of elementary functions and offer simpler and more accessible treatments of the physics of inertial motion than solutions written in terms of elliptic integrals [27].

Contributions of this paper include: (a) derivation and justification of the weakly spheroidal approximation, (b) complete identification, classification, naming, description, and illustration of the sixteen classes of inertial motion, including one new class (circumpolar waves), (c) discussion of the rotational/time-reversal symmetry relationships between classes, (d) derivation and validation of small-amplitude approximations for the four main classes and one degenerate class, and (e) calculations of experimentally relevant frequencies, zonal drifts, and latitude ranges of these five classes.

II. EQUATIONS OF MOTION

A. Normally Rotating Earth

To describe motion on the earth's spheroidal surface, we adopt the geodetic coordinate system (Fig. 2) that describes the reference spheroid used in terrestrial cartography, geodesy, satellite navigation, and the global positioning system (GPS) [29–31]. This spheroid has equatorial radius $a = 6378.137$ km, polar radius $b = 6356.752$ km, eccentricity

$$e = \frac{\sqrt{a^2 - b^2}}{a} = 0.08182, \tag{1}$$

angular velocity of rotation $\mathbf{\Omega} = \Omega\hat{z}$, and angular speed $\Omega = 7.292 \times 10^{-5}$ rad/s. Here, the unit vector $\hat{\mathrm{z}}$ is aligned with the earth's rotation axis and points toward the north pole [28]. The orthogonal unit vectors $\hat{\phi}$, $\hat{\theta}$, and $\hat{\mathrm{n}}$ respectively point horizontally east, horizontally north, and vertically up (normal to the surface).

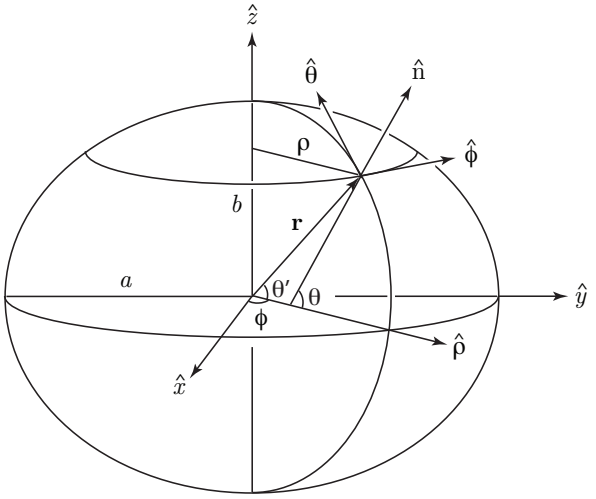

FIG. 2. Geodetic coordinates used to specify points on the surface of the earth, treated as a spheroid with equatorial radius a and polar radius b. As viewed by an observer in the rotating frame, the unit vectors $\hat{\mathrm{x}}$, $\hat{\mathrm{y}}$, and $\hat{\mathrm{z}}$ are stationary, with $\hat{\mathrm{x}}$ and $\hat{\mathrm{y}}$ marking specific geographical points on the equator and $\hat{\mathrm{z}}$ marking the north pole. Shown for a point on the surface are its position vector $\mathbf{r}$, its geodetic latitude θ, its geocentric latitude θ', its longitude ϕ, and its distance ρ from the axis of rotation, with orthogonal unit vectors $\hat{\phi}$, $\hat{\theta}$, and $\hat{\mathrm{n}}$ respectively pointing east, north, and up, and the unit vector $\hat{\rho}$ directed along the equatorial projection of $\mathbf{r}$. The difference between a and b is exaggerated to illuminate the difference between the geocentric and geodetic latitudes.

The geodetic coordinates of a point on the earth's surface are its longitude ϕ, measured eastward from the prime meridian, and its geodetic latitude θ, measured northward between the equatorial plane and the normal direction (Fig. 2). The geodetic latitude θ differs from the geocentric latitude θ', the angle measured northward between the equatorial plane and the position vector $\mathbf{r}$. The word "latitude," when used without qualification, refers to the geodetic latitude θ.

As seen by an observer in a reference frame S that rotates with the earth, the velocity of a hockey puck that slides horizontally along the earth's surface is given by

$$(\mathbf{v})_S = v_\phi\hat{\phi} + v_\theta\hat{\theta}. \tag{2}$$

This velocity has eastward and northward components that are given respectively by [28]

$$v_\phi = \rho\dot{\phi} \tag{3a}$$

$$v_\theta = R\dot{\theta}, \tag{3b}$$

where the overdot denotes a time derivative,

$$\rho = \frac{a\cos\theta}{\sqrt{1-e^2\sin^2\theta}} \tag{4a}$$

is the distance from the earth's axis of rotation, and

$$R = \frac{\left(1-e^2\right)a}{\left(1-e^2\sin^2\theta\right)^{3/2}} \tag{4b}$$

is the earth's meridional radius of curvature, measured along a line of longitude.

In the rotating frame S, four forces act on a puck that moves without friction on the surface of a smooth spheroidal planet; the gravitational force, the normal force, the centrifugal force, and the Coriolis force. For spheroidal planets that rotate at their stable angular speeds, as the earth does, the vector sum of the gravitational and centrifugal forces, called the apparent gravitational force, is normal to the planet's surface. The normal, Coriolis, and apparent gravitational forces are perpendicular to $\mathbf{v}_S$ and do no net work on the puck. The kinetic energy measured in the rotating frame is therefore conserved [16],

$$(T)_S = \frac{1}{2}m(v)_S^2, \tag{5}$$

where m is the puck's mass and

$$(v)_S = \sqrt{v_\phi^2 + v_\theta^2} \tag{6}$$

is its constant speed in this frame.

For a rotating spherical planet, the apparent gravitational force is not normal to the planet's surface and kinetic energy is conserved instead in the inertial frame S_0, which leads to essential differences between the motion on spherical and spheroidal earths [16]. Correct conclusions regarding the conservation of kinetic energy and correct descriptions of motion on the earth's surface therefore rely crucially on the earth's spheroidal deformations.

The axial angular momentum of a puck that moves without friction on the surface of a spheroidal planet is conserved in the inertial frame S_0 because the torques on the puck have no axial components. As seen by an observer in this frame, the puck's velocity is

$$(\mathbf{v})_{S_0} = (\mathbf{v})_S + \Omega\rho\,\hat{\phi} \tag{7a}$$

$$= (\Omega\rho + v_\phi)\,\hat{\phi} + v_\theta\hat{\theta}, \tag{7b}$$

where the eastward component includes the earth's eastward tangential velocity, $\Omega\rho\hat{\phi}$. Therefore, the axial angular momentum in the inertial frame is given by [16]

$$(L_z)_{S_0} = m\rho\,(\Omega\rho + v_\phi)\,. \tag{8}$$

We now use Eqs. (5) and (8) to construct equations of motion. We define a dimensionless puck speed in the rotating frame by

$$\varepsilon = \frac{(v)_S}{\Omega a}, \tag{9a}$$

where Ωa is the earth's tangential speed at the equator. We also define the puck's dimensionless axial angular momentum in the inertial frame as

$$\mathcal{L} = \frac{(L_z)_{S_0}}{ma^2\Omega}, \tag{9b}$$

where $ma^2\Omega$ is the angular momentum in the inertial frame for a puck that is at rest at the equator in the rotating frame. As will be seen below, the values of the dimensionless constants ε and $\mathcal{L}$ determine the behavior of the puck. Combining Eqs. (3) with Eqs. (6)-(9) gives equations of motion for $\phi(t)$ and $\theta(t)$ for a stably rotating planet of arbitrary eccentricity e,

$$\mathcal{L} = \frac{\rho^2}{a^2\Omega}\left(\Omega + \dot{\phi}\right) \tag{10a}$$

$$\varepsilon^2 = \frac{\rho^2\dot{\phi}^2 + R^2\dot{\theta}^2}{a^2\Omega^2}. \tag{10b}$$

According to Eqs. (4), the eccentricity corrections to Eqs. (10) are of relative order $e^2 = 0.0067$ for the earth's eccentricity of Eq. (1). Ignoring these corrections reduces Eqs. (10) to [18–26, 28]

$$\mathcal{L} = \left(1 + \frac{\dot{\phi}}{\Omega}\right)\cos^2\theta \tag{11a}$$

$$\varepsilon^2 = \frac{\dot{\phi}^2}{\Omega^2}\cos^2\theta + \frac{\dot{\theta}^2}{\Omega^2}. \tag{11b}$$

These coupled ordinary first-order nonlinear differential equations describe the latitude $\theta(t)$ and longitude $\phi(t)$ for a wide variety of behaviors for a puck that slides without friction on the surface of a weakly spheroidal planet that rotates at its stable angular speed, with ε and $\mathcal{L}$ serving as convenient constants of the motion. Solutions to Eqs. (11) agree with solutions to Eqs. (10) to within 1%, consistent with the neglect of terms of relative order $e^2 = 0.0067$. Such eccentricity corrections can also be ignored in the metric coefficients in spheroidal coordinates [41, Sec. 4.12]. Ignoring these corrections in Eqs. (3) gives the associated velocity components

$$v_\phi = a\dot{\phi}\cos\theta \tag{12a}$$

$$v_\theta = a\dot{\theta}. \tag{12b}$$

Although we have omitted spheroidal corrections of order e^2 in Eqs. (11), and although the eccentricity e appears nowhere in these equations, they do not describe motion on a spherical planet. They instead describe motion on a weakly spheroidal planet whose spheroidal deformations neutralize the centrifugal force and demand

conservation of kinetic energy in the rotating frame, as expressed in Eq. (11b). To account for the influence of the centrifugal force on a rotating spherical planet, this equation must be modified to conserve kinetic energy in the inertial frame, which leads to profound differences in the motion [16]. Thus, although Eqs. (11) ignore spheroidal corrections of order e^2, they do account for spheroidal deformations through energy conservation.

Equations (11) can be rearranged to produce equations of motion that are convenient for numerical integration,

$$\frac{\dot\phi}{\Omega} = \mathcal{L}\sec^2\theta - 1 \tag{13a}$$

$$\frac{\dot\theta^2}{\Omega^2} = \varepsilon^2 - (\mathcal{L}\sec\theta - \cos\theta)^2\,. \tag{13b}$$

Rearranging Eq. (11a) gives Eq. (13a), and substituting this result into Eq. (11b) gives Eq. (13b), a first-order ordinary nonlinear differential equation for the latitude $\theta(t)$. This equation agrees with Eq. (11a) of Ripa [19], with Eq. (6) of Pennell and Seiter [27], and with Eq. (5.1) of Paldor & Sigalov [23], apart from an additive constant that can be absorbed into the (constant) energy term (ε^2). Once a solution for $\theta(t)$ has been found from Eq. (13b), the longitude $\phi(t)$ follows from Eq. (13a).

In the following sections, we use three measures to characterize the puck's motion. For both periodic and nonperiodic motions, we consider the latitude range $\Delta\theta = \theta_{\max} - \theta_{\min}$, defined as the difference between the maximum and minimum latitudes. For periodic motions with period τ, we also consider the zonal drift $\Delta\phi = \phi(\tau) - \phi(0)$ in the rotating frame [24, 25] and the angular frequency $\omega = 2\pi/\tau$ of oscillations.

B. Counter-rotating Earth

Consideration of motion on a counter-rotating earth facilitates understanding of circumpolar circles and waves (Secs. VII and IX). We consider an earth that rotates westward instead of eastward, with $\hat{\mathrm{z}}$ still pointing north and with the earth's angular velocity $\mathbf{\Omega} = -\Omega\hat{\mathrm{z}}$ pointing south. We consider an observer in the frame S' of this counter-rotating earth (Fig. 2). As seen by an observer in this frame, the puck's velocity is

$$(\mathbf{v})_{S'} = (\mathbf{v})_{S_0} + \Omega\rho\,\hat{\phi} \tag{14a}$$

$$= (2\Omega\rho + v_\phi)\,\hat{\phi} + v_\theta\hat{\theta}, \tag{14b}$$

where the second equality follows from Eq. (7b).

In frame S', it is convenient to define the longitude by

$$\phi' = -2\Omega t - \phi, \tag{15}$$

with ϕ' increasing toward the west (in contrast with ϕ, which increases toward the east) and with ϕ' marking specific geographic locations on the counter-rotating earth. Combining Eqs. (14b) and (15) and imposing the weakly spheroidal approximation gives the associated puck velocity

$$(\mathbf{v})_{S'} = -a\dot\phi'\cos\theta\,\hat\phi + a\dot\theta\hat\theta \tag{16a}$$

and puck speed

$$(v)_{S'} = a\sqrt{\dot\phi'^2\cos^2\theta + \dot\theta^2}. \tag{16b}$$

In the counter-rotating frame S', we also define a dimensionless puck speed

$$\varepsilon' = \frac{(v)_{S'}}{\Omega a} \tag{17a}$$

and a dimensionless angular momentum about the $-\hat{\mathrm{z}}$ axis,

$$\mathcal{L}' = -\mathcal{L}. \tag{17b}$$

The resulting weakly spheroidal equations in the counter-rotating frame are

$$\mathcal{L}' = \left(1 + \frac{\dot\phi'}{\Omega}\right)\cos^2\theta \tag{18a}$$

$$\varepsilon'^2 = \frac{\dot\phi'^2}{\Omega^2}\cos^2\theta + \frac{\dot\theta^2}{\Omega^2}, \tag{18b}$$

where Eq. (18a) follows from Eq. (11a) and where Eq. (18b) follows from Eqs. (16b) and (17a). Equations (11), (15), and (18b) imply the relationship

$$\varepsilon'^2 = \varepsilon^2 + 4\mathcal{L}. \tag{19}$$

Equations (18) have the same form as Eqs. (11). Consequently, the transformations given by Eqs. (15), (17b), and (19) allow solutions of Eqs. (11) to be mapped to solutions of Eqs. (18).

Reversing the direction of the earth's rotation, reversing the sign of the axial angular momentum, measuring longitude westward instead of eastward, and leaving the latitude unchanged yields the same equations of motion on the earth's surface, Eqs. (18), as the equations for the normally rotating earth, Eqs. (11). On the counter-rotating earth, the horizontal component of the Coriolis force acts toward the *left* in the northern hemisphere and toward the *right* in the southern hemisphere, which is opposite to its behavior on the normally rotating earth.

III. MOTION CLASSIFICATION

The purpose of this paper is to classify the inertial motions of a puck that moves without friction on the surface of a weakly spheroidal earth that rotates normally at its stable angular speed. This classification relies on the values of two conserved quantities, the puck's dimensionless speed ε in the rotating frame and the puck's dimensionless angular momentum $\mathcal{L}$ in the inertial frame. Figure 3

shows the associated 2D state space that forms the basis for the classification. In contrast with Fig. 7 of Cushman-Roisin [17] and Fig. 3 of Ripa [19], Fig. 3 conveniently considers $\mathcal{L}$ as a function of ε and includes information about the specific extrema that apply in each region.

The initial conditions $\theta(0)$, $\dot\theta(0)$, $\phi(0)$, and $\dot\phi(0)$ determine the values of the conserved quantities ε and $\mathcal{L}$ [28]. These values determine the point in state space in Fig. 3 and the associated class of motion. Each point in Fig. 3 represents motion of a single class. Although a particular set of values of ε and $\mathcal{L}$ is generally shared by a family of related initial conditions, once the values of ε and $\mathcal{L}$ are established by the initial conditions, the associated class of motion is uniquely determined by Fig. 3.

As a first step in constructing Fig. 3, we use Eqs. (11) to determine the allowed range of $\mathcal{L}$ for fixed $\varepsilon \geq 0$. The maximum value $\mathcal{L} = 1+\varepsilon$ occurs for eastward motion at the equator, with $\theta = \dot\theta = 0$ and $\dot\phi = \varepsilon\Omega$ (Fig. 3, EF). The minimum value of $\mathcal{L}$ occurs for westward motion with $\dot\theta = 0$, $\dot\phi = -\varepsilon\Omega/\cos\theta$, and $\mathcal{L} = \cos^2\theta - \varepsilon\cos\theta$. To find this minimum, we set

$$\frac{d\mathcal{L}}{d\theta} = \sin\theta\,(\varepsilon - 2\cos\theta) = 0. \tag{20}$$

Setting $\sin\theta = 0$ gives $\mathcal{L} = 1-\varepsilon$ (Fig. 3, EF′). Setting $\varepsilon - 2\cos\theta = 0$ gives a lower minimum $\mathcal{L} = -\varepsilon^2/4$ that is valid for $\varepsilon \leq 2$ to ensure that $\cos\theta = \varepsilon/2 \leq 1$ (Fig. 3, CE′). Thus, the range of $\mathcal{L}$ is $-\varepsilon^2/4 \leq \mathcal{L} \leq 1+\varepsilon$ for $\varepsilon \leq 2$, and $1-\varepsilon \leq \mathcal{L} \leq 1+\varepsilon$ for $\varepsilon > 2$ (Fig. 3).

The next step in constructing the state space is to examine latitude extrema $\theta = \theta^*$ given by setting $\dot\theta = 0$ in Eq. (13b), which yields a quartic polynomial equation in $\cos\theta^*$ with four solutions,

$$\cos\theta_1^* = +\frac{\varepsilon}{2} + \sqrt{\mathcal{L} + \frac{\varepsilon^2}{4}} \tag{21a}$$

$$\cos\theta_2^* = -\frac{\varepsilon}{2} + \sqrt{\mathcal{L} + \frac{\varepsilon^2}{4}} \tag{21b}$$

$$\cos\theta_3^* = +\frac{\varepsilon}{2} - \sqrt{\mathcal{L} + \frac{\varepsilon^2}{4}} \tag{21c}$$

$$\cos\theta_4^* = -\frac{\varepsilon}{2} - \sqrt{\mathcal{L} + \frac{\varepsilon^2}{4}}. \tag{21d}$$

These extrema must be real and must satisfy $0 \leq \cos\theta^* \leq 1$ over the latitude range $-\pi/2 \leq \theta^* \leq \pi/2$.

We now determine the ranges of $\mathcal{L}$ that satisfy these two conditions for fixed $\varepsilon \geq 0$ for the extrema θ_1^*, θ_2^*, and θ_3^*, noting that θ_4^* fails to satisfy these conditions except for the degenerate case $\varepsilon = \mathcal{L} = 0$, which is covered by the other extrema. We take θ_1^*, θ_2^*, and θ_3^* to be positive, corresponding to northern latitudes. Because $\cos(-\theta^*) = \cos\theta^*$, the southern latitudes $-\theta_1^*$, $-\theta_2^*$, and $-\theta_3^*$ also satisfy Eqs. (21a)-(21c).

To ensure that θ_1^* is real, we must have $\mathcal{L} \geq -\varepsilon^2/4$, for which $\cos\theta_1^* \geq 0$. To ensure that $\cos\theta_1^* \leq 1$, we must have $\mathcal{L} \leq 1-\varepsilon$ and $\epsilon \leq 2$. Hence, the extrema $\theta = \pm\theta_1^*$ apply for $-\varepsilon^2/4 \leq \mathcal{L} \leq 1-\varepsilon$ and $\varepsilon \leq 2$ (Fig. 3, diagonal shading).

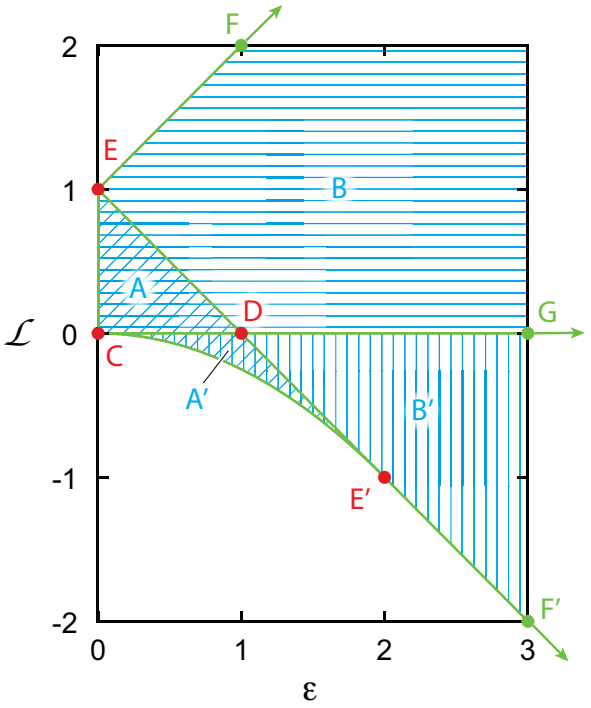

FIG. 3. State space of values of the dimensionless axial angular momentum $\mathcal{L}$ in the inertial frame [Eq. (9b)] and the dimensionless speed ε in the rotating frame [Eq. (9a)] for a puck that moves on the frictionless surface of a weakly spheroidal planet that rotates at its stable angular speed. Regions of diagonal, horizontal, and vertical cyan shading respectively indicate where latitude extrema θ_1^*, θ_2^*, and θ_3^* apply [Eqs. (21)]. Two extrema (θ_1^*, θ_2^*) apply in region A, two (θ_1^*, θ_3^*) in region A′, one (θ_2^*) in region B, and one (θ_3^*) in region B′. Red dots denote junctions C, D, E, and E′. Green traces denote region boundaries. Green dots and arrows denote extension points F, F′, and G, where regions B and B′ and region boundaries EF, E′F′, and DG extend indefinitely beyond the frame of the diagram. The regions, boundaries, and junctions comprise sixteen classes of inertial motion that are summarized in Table I and illustrated in Fig. 4.

To ensure that $\cos\theta_2^* \geq 0$, we must have $\mathcal{L} \geq 0$, which also ensures that θ_2^* is real. To ensure that $\cos\theta_2^* \leq 1$, we must have $\mathcal{L} \leq 1+\varepsilon$. Hence, the extrema $\theta = \pm\theta_2^*$ apply for $0 \leq \mathcal{L} \leq 1+\varepsilon$ and $\varepsilon \geq 0$ (Fig. 3, horizontal shading).

To ensure that θ_3^* is real, we must have $\mathcal{L} \geq -\varepsilon^2/4$. To ensure that $\cos\theta_3^* \geq 0$, we must have $\mathcal{L} \leq 0$. At a particular value of ε, the maximum value of $\cos\theta_3^*$ is reached for $\mathcal{L} = -\varepsilon^2/4$, for which $\cos\theta_3^* = \varepsilon/2$. Thus $\cos\theta_3^* \leq 1$ for $\varepsilon \leq 2$. To ensure that $\cos\theta_3^* \leq 1$ for $\varepsilon \geq 2$, we must instead have $\mathcal{L} \geq 1-\varepsilon$. Thus, for $\varepsilon \leq 2$, the extrema $\theta = \pm\theta_3^*$ apply for $-\varepsilon^2/4 \leq \mathcal{L} \leq 0$, and for $\varepsilon \geq 2$, these extrema apply for $1-\varepsilon \leq \mathcal{L} \leq 0$ (Fig. 3, vertical shading).

Figure 3 identifies sixteen classes of inertial motion: four main classes corresponding to regions A, A′, B, and B′; eight degenerate classes corresponding to regional boundaries CD, CE, CE′, DE, DE′, EF, E′F′, and DG;

TABLE I. List of sixteen classes of inertial motion labeled by their *CorioVis* demonstration numbers [32], together with their locations in state space (Fig. 3) and latitude ranges. Main classes, degenerate classes, and doubly-degenerate classes are listed respectively in bold, italic, and Roman typefaces. The latitude extrema θ_1^*, θ_2^*, and θ_3^* are defined in Eqs. (21). The sixteen classes are illustrated in Fig. 4.

Inertial Motion Class	**State Space**	**Latitude Range**
C1. Stationary at pole	Junction C	$\theta = \pm\pi/2$
C2. *Stationary at midlatitude*	Boundary CE	$\theta = \cos^{-1}\sqrt{\mathcal{L}}$
C3. **Nonpolar circles**	Region A	$\theta_1^* \le \lvert\theta\rvert \le \theta_2^*$
C4. *Polar circles*	Boundary CD	$\cos^{-1}\varepsilon \le \lvert\theta\rvert \le \pi/2$
C5. **Circumpolar circles**	Region A′	$\theta_1^* \le \lvert\theta\rvert \le \theta_3^*$
C6. *Westward at midlatitude*	Boundary CE′	$\theta = \cos^{-1}(\varepsilon/2)$
C7. Stationary at equator	Junction E	$\theta = 0$
C8. *Nonpolar asymptote*	Boundary DE	$0 < \lvert\theta\rvert \le \theta_2^*$
C9. Polar asymptote	Junction D	$0 < \lvert\theta\rvert \le \pi/2$
C10. *Circumpolar asymptote*	Boundary DE′	$0 < \lvert\theta\rvert \le \theta_3^*$
C11. Westward at equator	Junction E′	$\theta = 0$
C12. *Eastward at equator*	Boundary EF	$\theta = 0$
C13. **Nonpolar waves**	Region B	$\lvert\theta\rvert \le \theta_2^*$
C14. *Polar waves*	Boundary DG	$\lvert\theta\rvert \le \pi/2$
C15. **Circumpolar waves**	Region B′	$\lvert\theta\rvert \le \theta_3^*$
C16. *Fast westward at equator*	Boundary E′F′	$\theta = 0$

and four doubly degenerate classes corresponding to junctions C, D, E, and E′. We assign labels C1-C16 to these sixteen classes, which are listed in Table I, are illustrated in Fig. 4, are described in the text below, and are visualized in sixteen *CorioVis* demonstrations numbered C1-C16 [32]. Main classes, degenerate classes, and doubly-degenerate classes are listed respectively in bold, italic, and Roman typefaces.

Because the degenerate and doubly degenerate classes lie along lines and points in the 2D state space (Fig. 3) and because these lines and points occupy no area in this space, randomly chosen initial conditions will never produce a degenerate or a doubly degenerate class of motion. Although these degenerate classes are needed for completeness and might be observable with carefully chosen initial conditions, random initial conditions and naturally occurring motion will always fall into one of the four main classes, which occupy regions in state space.

Figure 4 is our 2D classification scheme for inertial motions. We call classes that cross the equator "waves" (row 4), classes that asymptotically approach the equator "asymptotes" (row 3), and classes that avoid the equator "circles" (row 2). The axial angular momentum $\mathcal{L}$ decreases from left to right along each row; the middle column is for $\mathcal{L} = 0$. This classification scheme emphasizes the uniqueness of each class and its relationship with other classes. We now summarize the properties of each of the sixteen classes.

C1. Stationary at pole: At junction C in Fig. 3, the values $\varepsilon = \mathcal{L} = 0$ imply that the puck is stationary at the north or south pole.

C2. *Stationary at midlatitude*: Along boundary CE, the puck is stationary in the rotating frame ($\varepsilon = 0$). The puck resides at latitude $\theta = \cos^{-1}\sqrt{\mathcal{L}}$, found by setting $\dot{\phi} = 0$ in Eq. (11a). In moving from C ($\mathcal{L} = 0$) to E ($\mathcal{L} = 1$) along boundary CE, the puck's latitude moves from a pole ($\theta = \pm\pi/2$) to the equator ($\theta = 0$). This movement reflects the increase in the angular momentum in the inertial frame that is associated with increasing the distance between the puck and the earth's rotation axis, for a puck of fixed angular speed Ω.

C3. **Nonpolar Circles**: Region A is the interior of triangle CDE. In this region in the rotating frame, the puck is confined either to the northern hemisphere, where it executes westward-drifting clockwise circles in the latitude range $\theta_1^* \le \theta \le \theta_2^*$, or to the southern hemisphere, where it executes westward-drifting counterclockwise circles in the latitude range $-\theta_2^* \le \theta \le -\theta_1^*$; the latitude extrema are given in Eqs. (21). Nonpolar circles do not pass through or around a pole and are confined to a single hemisphere. Referred to as "inertial circles," they are the best known example of inertial oscillations and have been observed in ocean currents [8, 33–38].

C4. *Polar circles*: On the CD boundary in the rotating frame, $\mathcal{L} = 0$ and the puck executes westward-drifting circles that are confined to a single hemisphere and are similar to nonpolar circles except that each circle crosses directly over a pole. As discussed in Sec. VI, when viewed in the inertial frame, polar circles become polar oscillations along a great circle. *CorioVis* supplies views in both frames by using the "f" key to toggle between frames.

C5. **Circumpolar Circles**: Region A′ is the interior of region CDE′. In this region in the rotating frame, the

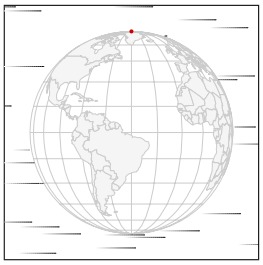

C1. Stationary at pole
(0, 0)

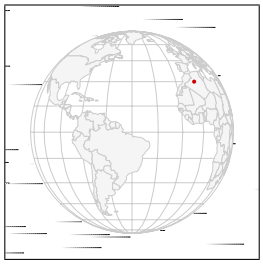

C2. *Stationary at midlatitude*
(0, +0.8)

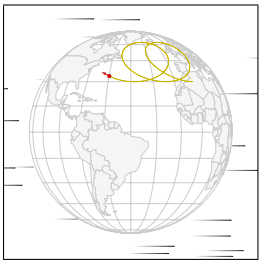

C3. **Nonpolar circles**
(0.4, +0.4)

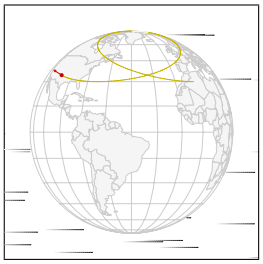

C4. *Polar circles*
(0.9, 0)

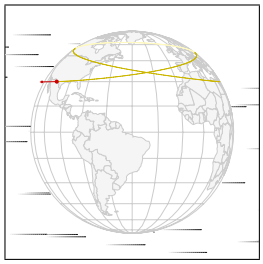

C5. **Circumpolar circles**
(1.3, −0.4)

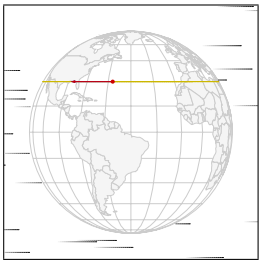

C6. *Westward at midlatitude*
(1.7, −.8)

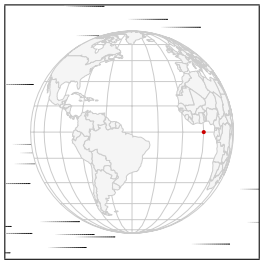

C7. Stationary at equator
(0, 1)

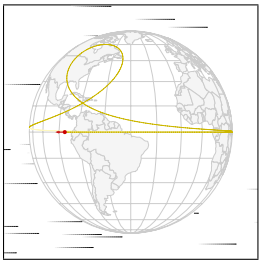

C8. *Nonpolar asymptote*
(0.5, +0.5)

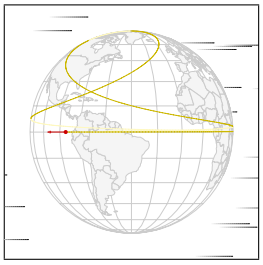

C9. Polar asymptote
(1, 0)

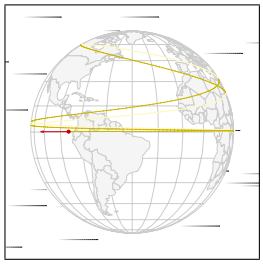

C10. *Circumpolar asymptote*
(1.5, −0.5)

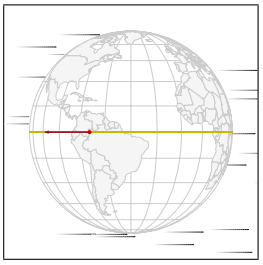

C11. Westward at equator
(2, −1)

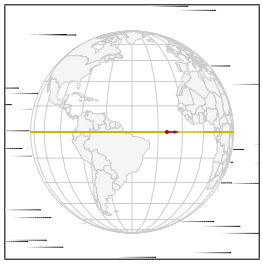

C12. *Eastward at equator*
(0.5, +1.5)

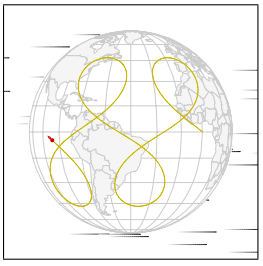

C13. **Nonpolar waves**
(0.4, +0.7)

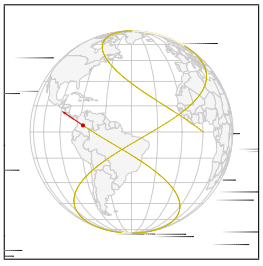

C14. *Polar waves*
(1.2, 0)

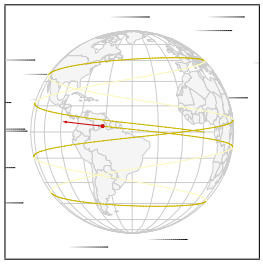

C15. **Circumpolar waves**
(1.7, −0.7)

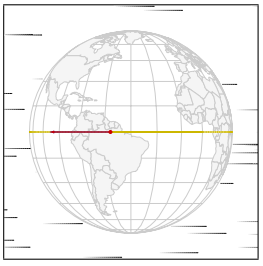

C16. *Fast westward at equator*
(2.5, −1.5)

FIG. 4. Our 2D classification scheme for inertial motions of a puck that slides on the earth's stably rotating spheroidal surface, assumed frictionless, as seen by an observer in the rotating frame. Shown are screenshots of *CorioVis* visualizations labeled by their *CorioVis* demonstration numbers [32] and values of $(\varepsilon,\ \mathcal{L})$. Puck trajectories are shown in yellow. Red dots denote final puck positions and red arrows denote final puck velocities. Typefaces mirror those in Table I.

puck executes westward-drifting circles that are confined to a single hemisphere and are similar to nonpolar circles except that each circle circumscribes a pole.

C6. *Westward at midlatitude*: Along boundary CE′, $\mathcal{L} = -\varepsilon^2/4$ and the puck travels due west in the rotating frame.

C7. Stationary at equator: At junction E, $\varepsilon = 0$ and $\mathcal{L} = 1$ and the puck is stationary at the equator in the rotating frame.

C8. *Nonpolar asymptote*: Along boundary DE, $\mathcal{L} =$

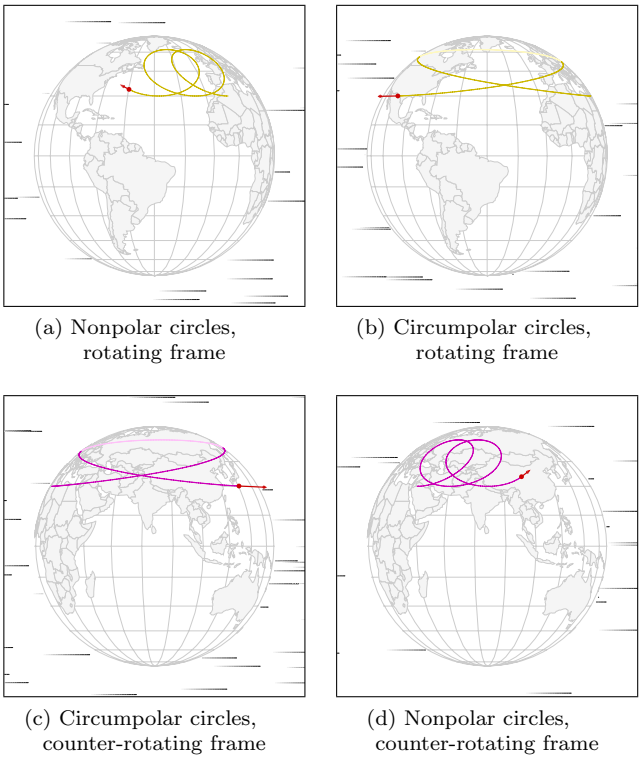

(a) Nonpolar circles, rotating frame

(b) Circumpolar circles, rotating frame

(c) Circumpolar circles, counter-rotating frame

(d) Nonpolar circles, counter-rotating frame

FIG. 5. *CorioVis* screenshots of nonpolar circles (a) and circumpolar circles (b) as seen in the rotating frame (Fig. 4, classes C3 and C5) and their respective trajectories (c) and (d) as seen in the counter-rotating frame. Panels (a) and (c) are the same trajectories and have the same initial conditions. The difference is that they are viewed from two different frames of reference. *CorioVis* demo C3 supplies both views by using the "f" key to toggle between reference frames [32]. Similarly with panels (b) and (d) (*CorioVis* demo C5). The circumpolar circles of panel (c) follow from a time reversal of the circumpolar circles of panel (b) and the nonpolar circles of panel (d) follow from a time reversal of the nonpolar circles of panel (a).

$1-\varepsilon$ and the puck approaches the equator asymptotically traveling west in the rotating frame after completing at most one loop. Whether it executes a complete loop or only a part of a loop depends on the initial conditions. The loop is clockwise in the northern hemisphere and counterclockwise in the southern hemisphere, and does not pass through or around a pole.

C9. Polar asymptote: At $\mathcal{L} = 0$, junction D is the $\varepsilon \to 1$ limit of the nonpolar asymptote, so in the rotating frame, the puck executes at most one loop that passes through a pole, then approaches the equator asymptotically traveling west.

C10. *Circumpolar asymptote*: Along boundary DE′, $\mathcal{L} = 1 - \varepsilon$ and the puck approaches the equator asymptotically traveling west in the rotating frame after completing at most one loop that circumscribes a pole.

C11. Westward at equator: At junction E′, $\varepsilon = 2$ and $\mathcal{L} = -1$, and the puck is confined to the equator. It travels west in the rotating frame and is stationary in the counter-rotating frame.

C12. *Eastward at equator*: At boundary EF, $\mathcal{L} = 1+\varepsilon$ and the puck is confined to the equator traveling east. At E, the puck is stationary at the equator in the rotating frame. As ε increases, the eastward speed of the puck increases in this frame.

C13. **Nonpolar Waves**: In region B in the rotating frame, the puck visits both hemispheres and oscillates symmetrically across the equator, executing loops in both hemispheres. These loops circulate clockwise in the northern hemisphere and counterclockwise in the southern hemisphere, and do not pass through or around a pole.

C14. *Polar waves*: At junction DG in the rotating frame, the puck's behavior is similar to nonpolar waves except that the puck passes through both poles. Because $\mathcal{L} = 0$ for these waves, their motion is along a great circle when viewed in the inertial frame, but with non-constant speed, in a manner similar to the behavior of polar circles when viewed in the inertial frame.

C15. **Circumpolar Waves**: In region B′, the puck's behavior is similar to nonpolar waves except that the puck passes around both poles.

C16. *Fast westward at equator*: At boundary E′F′, the puck moves westward at the equator in both the rotating and counter-rotating frames.

All of the trajectories shown in the center column of Fig. 4 (classes C1, C4, C9, and C14) have $\mathcal{L} = 0$. For all of these trajectories, the puck either resides at a pole or passes through at least one pole. The reason is that setting $\theta = \pm\pi/2$ in Eq. (11a) gives $\mathcal{L} = 0$. Since $\mathcal{L}$ is a conserved quantity, any trajectory that resides at a pole or passes through at least one pole must have $\mathcal{L} = 0$.

All of the trajectories shown to the left of the center column of Fig. 4 have $\mathcal{L} > 0$ and all of the trajectories to the right have $\mathcal{L} < 0$. To illustrate the rotation symmetry of Sec. II B, we substitute values of (ε, $\mathcal{L}$) for each $\mathcal{L} > 0$ trajectory in Fig. 4 into Eqs. (17b) and (19) to find the values of (ε, $\mathcal{L}$) for the corresponding $\mathcal{L} < 0$ trajectory in Fig. 4. Each resulting pair of trajectories shares the same latitude range, and paired periodic trajectories share the same period of motion.

For example, we substitute the values (0.4, +0.4) for the nonpolar circles of Fig. 4, class C3 into Eqs. (17b) and (19) to find the values (1.3, −0.4) for the circumpolar circles of Fig. 4, class C5. Both share the same latitude range $\Delta\theta = 33°$ and period $\tau = 18$ hr.

Figure 5 emphasizes the rotation symmetry of these states by showing that nonpolar circles in the rotating frame (a) become circumpolar circles when viewed in the counter-rotating frame (c) and circumpolar circles in the rotating frame (b) become nonpolar circles when viewed in the counter-rotating frame (d). Thus, a set of initial conditions that produces clockwise, westward drifting, nonpolar inertial circles when viewed by an earthbound observer in the northern hemisphere of a normally rotating earth (a) produces counterclockwise, eastward drifting, circumpolar inertial circles when viewed by an

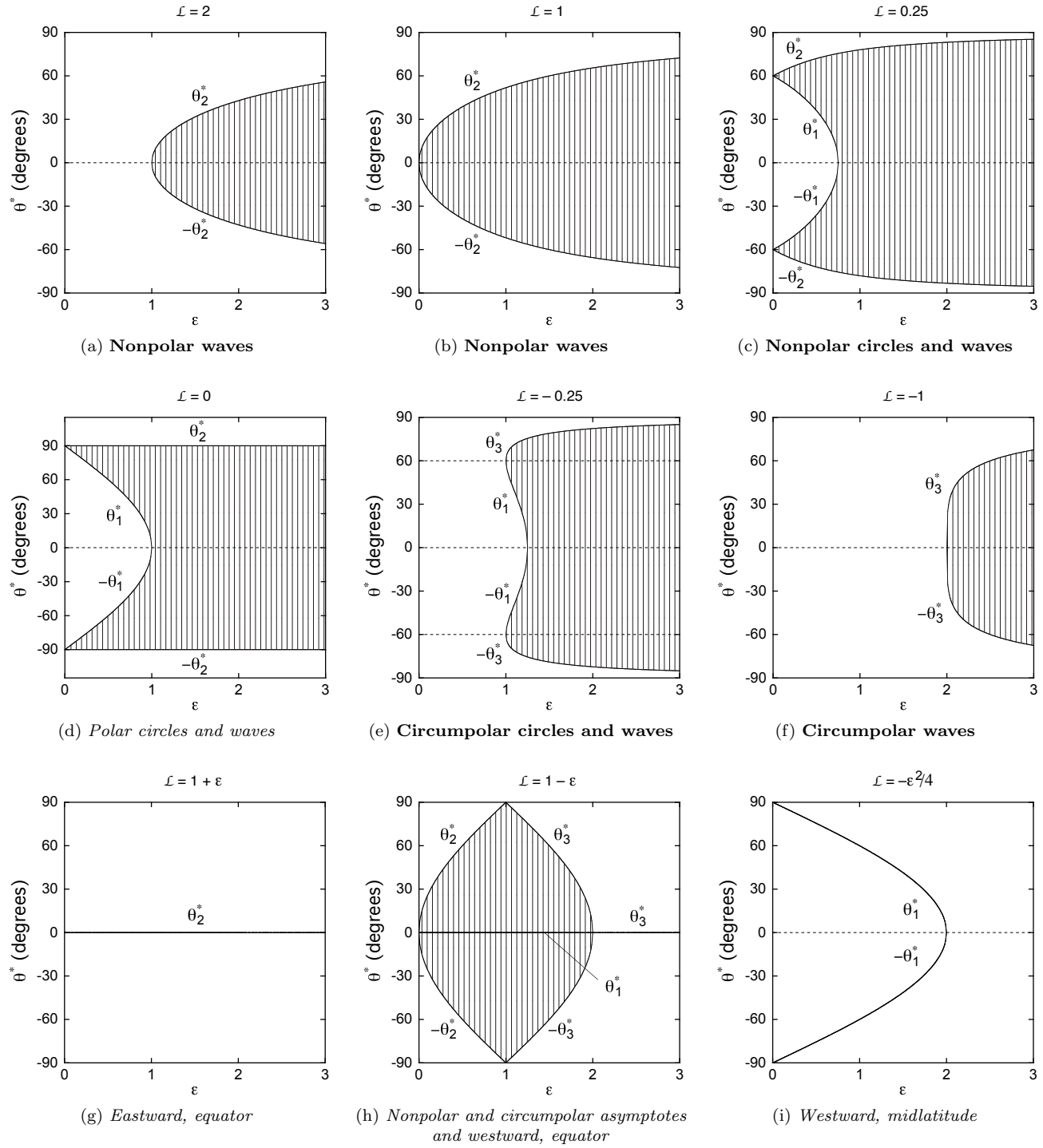

(a) **Nonpolar waves** (b) **Nonpolar waves** (c) **Nonpolar circles and waves**

(d) *Polar circles and waves* (e) **Circumpolar circles and waves** (f) **Circumpolar waves**

(g) *Eastward, equator* (h) *Nonpolar and circumpolar asymptotes and westward, equator* (i) *Westward, midlatitude*

FIG. 6. Latitudes visited (shaded regions) bounded by latitude extrema [solid traces, Eqs. (21)] as a function of ε for selected values of $\mathcal{L}$. The associated class or classes of inertial oscillations are listed below each panel, with typefaces mirroring those in Table I.

earth-bound observer in the northern hemisphere of a counter-rotating earth (c).

Figure 5 also shows that circumpolar circles in the counter-rotating frame (c) follow from circumpolar circles in the rotating frame (b) by reversing the flow of time - that is, by following the same trajectory at the same speed but in the reverse direction, on an earth that rotates backwards. Similarly, nonpolar circles in the counter-rotating frame (d) follow from nonpolar circles in the rotating frame (a) by reversing the time. Thus, the

rotation symmetry is a time-reversal symmetry.

IV. TRANSITIONS

To better understand the transitions between these sixteen classes of inertial motion, we consider latitude ranges as a function of ε in Fig. 6.

For $\mathcal{L} = 2$, Fig. 6(a) reflects eastward motion at the equator (boundary EF) for $\varepsilon = 1$ and nonpolar waves (region B) of increasing range for $\varepsilon > 1$.

For $\mathcal{L} = 1$, Fig. 6(b) reflects a stationary puck at the equator (junction E) for $\varepsilon = 0$ and nonpolar waves (region B) of increasing range for $\varepsilon > 0$.

For $\mathcal{L} = 0.25$, Fig. 6(c) reflects a stationary puck at midlatitude ($\pm 60°$, boundary CE) for $\varepsilon = 0$, nonpolar circles (region A) of increasing range for $0 < \varepsilon < 0.75$, a nonpolar asymptote (junction DE) for $\varepsilon = 0.75$, and nonpolar waves (region B) of increasing range for $\varepsilon > 0.75$.

For $\mathcal{L} = 0$, Fig. 6(d) reflects a stationary puck at a pole (junction C) for $\varepsilon = 0$, polar circles (boundary CD) of increasing range for $0 < \varepsilon < 1$, a polar asymptote (junction D) for $\varepsilon = 1$, and polar waves (boundary DG) for $\varepsilon > 1$.

For $\mathcal{L} = -0.25$, Fig. 6(e) reflects westward motion at midlatitude ($\pm 60°$, boundary CE$'$) for $\varepsilon = 1$, circumpolar circles (region A$'$) of increasing range for $1 < \varepsilon < 1.25$, a circumpolar asymptote (boundary DE$'$) for $\varepsilon = 1.25$, and circumpolar waves (region B$'$) of increasing range for $\varepsilon > 1.25$.

For $\mathcal{L} = -1$, Fig. 6(f) reflects westward motion at the equator (junction E$'$) for $\varepsilon = 2$ and circumpolar waves (region B$'$) of increasing range for $\varepsilon > 2$.

For $\mathcal{L} = 1 + \varepsilon$, Fig. 6(g) reflects a stationary puck at the equator (junction E) for $\varepsilon = 0$ and eastward motion at the equator (boundary EF) for $\varepsilon > 0$.

For $\mathcal{L} = 1 - \varepsilon$, Fig. 6(h) reflects a stationary puck at the equator (junction E) for $\varepsilon = 0$, nonpolar asymptotes (boundary DE) of increasing range for $0 < \varepsilon < 1$, a polar asymptote (junction D) for $\varepsilon = 1$, circumpolar asymptotes (boundary DE$'$) of decreasing range for $1 < \varepsilon < 2$, westward motion at the equator (junction E$'$) for $\varepsilon = 2$, and fast westward motion at the equator (boundary E$'$F$'$) for $\varepsilon > 2$.

For $\mathcal{L} = 1 - \varepsilon^2/4$, Fig. 6(i) reflects a stationary puck at a pole (junction C) for $\varepsilon = 0$, westward motion at midlatitude (boundary CE$'$) for $0 < \varepsilon < 2$, and westward motion at the equator (junction E$'$) for $\varepsilon = 2$.

V. NONPOLAR CIRCLES

In this section, we investigate small-amplitude nonpolar circles for the westward launch of Fig. 4, class C3. Small-amplitude nonpolar circles occur in region A of Fig. 3 near the CE boundary, where ε is small and the puck makes small westward-drifting circles about a line of latitude. We expand ϕ, θ, and $\mathcal{L}$ in powers of ε according to

$$\phi(t) = \phi_0 + \varepsilon\phi_1(t) + \varepsilon^2\phi_2(t) + \cdots \tag{22a}$$

$$\theta(t) = \theta_0 + \varepsilon\theta_1(t) + \varepsilon^2\theta_2(t) + \cdots \tag{22b}$$

$$\mathcal{L} = \mathcal{L}_0 + \varepsilon\mathcal{L}_1 + \varepsilon^2\mathcal{L}_2 + \cdots, \tag{22c}$$

where $\phi(0) = \phi_0$ is the initial longitude and θ_0 is the midlatitude, as discussed below.

We use the Taylor expansion

$$f(\theta) = f(\theta_0) + f'(\theta_0)(\theta - \theta_0) + \frac{1}{2}f''(\theta_0)(\theta - \theta_0)^2 + \cdots \tag{23}$$

to expand $f(\theta) = \cos^2\theta$, yielding

$$\cos^2\theta = \cos^2\theta_0 - \varepsilon\theta_1 \sin 2\theta_0 - \varepsilon^2\left(\theta_2 \sin 2\theta_0 + \theta_1^2 \cos 2\theta_0\right) + \cdots. \tag{24}$$

To order ε^0, Eq. (11a) gives

$$\mathcal{L}_0 = \cos^2\theta_0. \tag{25}$$

To order ε^1, Eq. (11a) yields

$$\mathcal{L}_1 = -\theta_1 \sin 2\theta_0 + \frac{\dot{\phi}_1}{\Omega}\cos^2\theta_0. \tag{26}$$

To order ε^2, Eq. (11b) yields

$$\Omega^2 = \dot{\phi}_1^2 \cos^2\theta_0 + \dot{\theta}_1^2. \tag{27}$$

The oscillatory solutions

$$\dot{\phi}_1(t) = -\frac{\Omega}{\cos\theta_0}\cos\omega t \tag{28a}$$

$$\dot{\theta}_1(t) = \Omega \sin\omega t \tag{28b}$$

satisfy Eq. (27), and describe motion for a westward launch. Integrating Eqs. (28) and imposing $\phi_1(0) = 0$ and $\theta_1(0) = -\Omega/\omega$ gives

$$\phi_1(t) = -\frac{\Omega}{\omega\cos\theta_0}\sin\omega t \tag{29a}$$

$$\theta_1(t) = -\frac{\Omega}{\omega}\cos\omega t. \tag{29b}$$

Inserting these into Eq. (26) gives

$$\mathcal{L}_1 = \cos\theta_0 \cos\omega t \left(\frac{2\Omega \sin\theta_0}{\omega} - 1\right). \tag{30}$$

Since $\mathcal{L}$ is a constant of the motion, $\mathcal{L}_1$ must also be a constant of the motion. Consequently, Eq. (30) implies

$$\mathcal{L}_1 = 0 \tag{31}$$

and an angular frequency of oscillations

$$\omega = 2\Omega \sin\theta_0. \tag{32}$$

This angular frequency is called the Coriolis parameter, and is positive in the northern hemisphere ($\theta_0 > 0$) and negative in the southern hemisphere ($\theta_0 < 0$) [19].

To order ε^2, Eq. (11a) yields

$$\mathcal{L}_2 = -\theta_1^2 \cos 2\theta_0 - \theta_2 \sin 2\theta_0 - \frac{\dot{\phi}_1}{\Omega}\theta_1 \sin 2\theta_0 + \frac{\dot{\phi}_2}{\Omega}\cos^2\theta_0 \tag{33}$$

To order ε^3, Eq. (11b) yields

$$\dot{\phi}_1\dot{\phi}_2 \cos^2\theta_0 + \dot{\theta}_1\dot{\theta}_2 = \frac{1}{2}\dot{\phi}_1^2\theta_1 \sin 2\theta_0. \tag{34}$$

Equations (28), (29), (33), and (34) yield

$$\dot{\phi}_2 = \frac{\omega}{\cos\theta_0}\theta_2 + \frac{\Omega}{\cos^2\theta_0}\left[\mathcal{L}_2 + \left(\frac{1}{2} + \frac{1}{4\sin^2\theta_0}\right)\cos^2\omega t\right], \tag{35}$$

and

$$\dot{\theta}_2 \tan\omega t - \omega\theta_2 = \frac{\Omega}{\cos\theta_0}\left(\mathcal{L}_2 + \frac{\cos^2\omega t}{4\sin^2\theta_0}\right). \tag{36}$$

Imposing the initial condition $\theta_2(0) = 0$ on Eq. (36) gives

$$\mathcal{L}_2 = -\frac{1}{4\sin^2\theta_0}, \tag{37}$$

whence Eq. (36) can be written as

$$\dot{\theta}_2 \tan\omega t - \omega\theta_2 = -\frac{\Omega^2 \sin^2\omega t}{\omega \sin 2\theta_0}. \tag{38}$$

This is a first-order linear non-homogeneous ordinary differential equation in $\theta_2(t)$. Its particular solution is

$$\theta_2(t) = -\frac{\Omega^2 \sin^2\omega t}{\omega^2 \sin 2\theta_0}, \tag{39}$$

whence

$$\dot{\theta}_2(t) = -\frac{\Omega^2 \sin 2\omega t}{\omega \sin 2\theta_0}. \tag{40}$$

Inserting Eqs. (37) and (39) into Eq. (35) gives

$$\dot{\phi}_2(t) = \frac{\Omega}{2\cos^2\theta_0}\left(\cos^2\omega t - \frac{\sin^2\omega t}{\sin^2\theta_0}\right). \tag{41}$$

Integrating Eq. (41) and imposing the initial condition $\phi_2(0) = 0$ gives

$$\phi_2(t) = -\frac{\Omega t}{4\sin^2\theta_0} + \frac{\Omega \sin 2\omega t}{2\omega \sin^2 2\theta_0}\left(1 + \sin^2\theta_0\right) \tag{42}$$

Combining results gives the longitude, latitude, and axial angular momentum of nonpolar circles to second order in the amplitude,

$$\phi(t) = \phi_0 - \frac{\varepsilon\Omega \sin\omega t}{\omega\cos\theta_0} - \frac{\varepsilon^2\Omega t}{4\sin^2\theta_0} + \frac{\varepsilon^2\Omega \sin 2\omega t}{2\omega \sin^2 2\theta_0}\left(1 + \sin^2\theta_0\right) \tag{43a}$$

$$\theta(t) = \theta_0 - \frac{\varepsilon\Omega}{\omega}\cos\omega t - \frac{\varepsilon^2\Omega^2 \sin^2\omega t}{\omega^2 \sin 2\theta_0} \tag{43b}$$

$$\mathcal{L} = \cos^2\theta_0 - \frac{\varepsilon^2}{4\sin^2\theta_0}, \tag{43c}$$

with angular frequency ω given by Eq. (32) and period given by $\tau = 2\pi/|\omega|$. Equations (43), which are valid to order ε^2, describe clockwise circles in the northern hemisphere ($\theta_0 > 0$, $\omega > 0$) and counterclockwise circles in the southern hemisphere ($\theta_0 < 0$, $\omega < 0$).

The time derivative of Eq. (43b),

$$\dot{\theta}(t) = \varepsilon\Omega \sin\omega t - \frac{\varepsilon^2\Omega^2 \sin 2\omega t}{\omega \sin 2\theta_0}, \tag{44}$$

vanishes at times $t = 0,\ \tau,\ 2\tau, \ldots$, when the puck travels west at latitude

$$\theta_{\text{west}} = \theta_0 - \varepsilon\Omega/\omega. \tag{45a}$$

This time derivative also vanishes at times $t = \tau/2,\ 3\tau/2, \ldots$, when the puck travels east at latitude

$$\theta_{\text{east}} = \theta_0 + \varepsilon\Omega/\omega, \tag{45b}$$

with $|\theta_{\text{east}}| > |\theta_{\text{west}}|$. The latitude range is given by

$$\Delta\theta = |\theta_{\text{east}} - \theta_{\text{west}}| = \frac{\varepsilon}{|\sin\theta_0|}. \tag{46}$$

The strength of the horizontal component of the Coriolis force increases with increasing $|\theta|$. The puck therefore experiences a stronger horizontal Coriolis force at $\theta = \theta_{\text{east}}$ than at $\theta = \theta_{\text{west}}$. The puck's speed is constant in the rotating frame, where it spends more time traveling west than east, and drifts westward during each cycle of its motion (Fig. 7). The third term on the right side of Eq. (43a) is responsible for this westward zonal drift, which is given by

$$\Delta\phi = \phi(\tau) - \phi(0) = -\frac{\pi\varepsilon^2}{4|\sin^3\theta_0|}. \tag{47}$$

Because of this westward drift, the meridional latitude θ_{m}, defined as the latitude at which the puck travels due north and due south ($\dot{\phi} = 0$), differs from the midlatitude θ_0, which is midway between θ_{west} and θ_{east}. Setting Eq. (11a) equal to Eq. (43c) with $\dot{\phi} = 0$ and $\theta = \theta_{\text{m}}$ gives

$$\cos^2\theta_{\text{m}} = \cos^2\theta_0 - \frac{\varepsilon^2}{4\sin^2\theta_0} \tag{48}$$

To lowest order in ε, this gives

$$\theta_{\text{m}} = \theta_0 + \frac{\varepsilon^2}{4\sin^2\theta_0 \sin 2\theta_0}. \tag{49}$$

Therefore, starting at the equator, one encounters θ_{west}, θ_0, θ_{m}, and θ_{east}, in that order. This ordering applies to nonpolar circles in the northern and southern hemispheres, which are mirror images of each other on either side of the equator (Fig. 7).

Equations (43), describing small-amplitude nonpolar circles for a westward launch, are algebraically simpler than small-amplitude nonpolar circles for a northward launch [19]. The first reason is that, for a westward

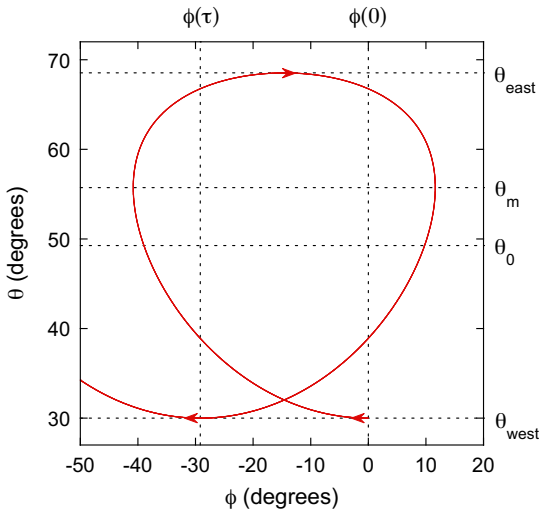

(a) **Nonpolar circles, northern hemisphere**

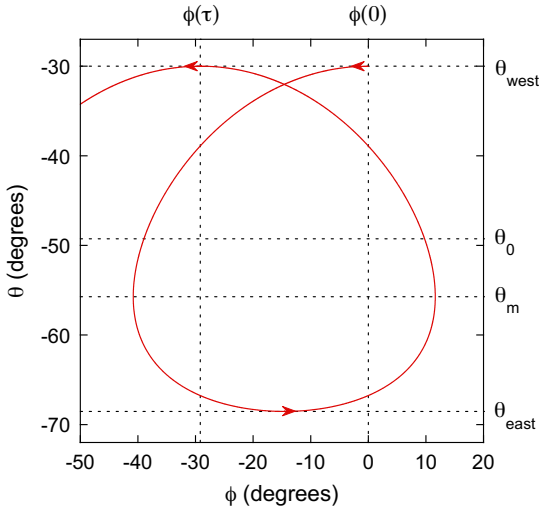

(b) **Nonpolar circles, southern hemisphere**

FIG. 7. Trajectories of nonpolar circles in the northern (a) and southern (b) hemispheres in the rotating frame showing the latitude θ vs. longitude ϕ obtained by integrating Eqs. (11) for a puck launched due west at dimensionless speed $\varepsilon = 0.5$ from initial latitude $\theta_{\rm west} = \pm 30^\circ$ and initial longitude $\phi(0) = 0$. Shown are the latitudes $\phi(\tau) = -29^\circ$ after one period $\tau = 17$ h of the motion, the midlatitudes $\theta_0 = \pm 49^\circ$ where the puck is halfway between $\theta_{\rm east}$ and $\theta_{\rm west}$, the meridional latitudes $\theta_{\rm m} = \pm 56^\circ$ where the puck travels due north and due south, and the maximum latitudes $\theta_{\rm east} = \pm 69^\circ$ where the puck travels due east. The images are distorted because they do not account for the convergence of longitude lines toward the poles ($\theta = \pm 90^\circ$).

launch, the latitude extrema given by Eqs. (45) occur at integer and half-integer multiples of the period τ. The second reason relates to the definition of the reference angle. The reference angle in Eqs. (43) is the midlatitude θ_0, midway between the latitude extrema. Using this reference angle, there are no second-order corrections to the

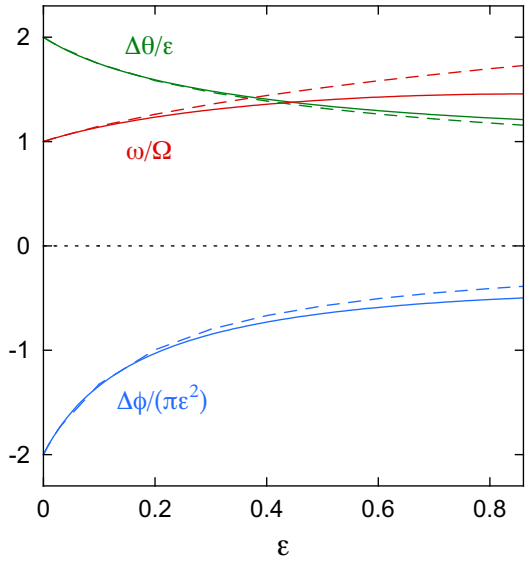

FIG. 8. Angular frequency ω, latitude range $\Delta\theta$ in radians, and zonal drift $\Delta\phi$ in radians vs. dimensionless speed ε for nonpolar circles in the rotating frame, where Ω is the earth's angular speed of rotation. Solid traces are numerical solutions of Eqs. (11) and dashed traces are small-amplitude approximations given by Eqs. (32), (46), and (47).

latitude extrema of Eqs. (45). In Ref. [19], the puck is launched northward from the meridional latitude, which is used as the reference angle. This requires second-order corrections to the latitude extrema.

Figure 8 compares the angular frequency ω, latitude range $\Delta\theta$, and zonal drift $\Delta\phi$ obtained from numerical integrations of Eqs. (11) (solid traces) with small-amplitude approximations given by Eqs. (32), (46), and (47) (dashed traces), vs. the dimensionless speed ε of nonpolar circles.

For the numerical integrations in Fig. 8, the puck is placed initially at latitude $\theta_{\rm west} = 30^\circ$ and is launched due west with initial speed $\varepsilon a\Omega$, where ε is its dimensionless speed, a is the earth's equatorial radius, and Ω is the earth's angular speed of rotation (Sec. II). Accordingly, the puck's initial velocity components are

$$v_\phi(0) = -\varepsilon a\Omega \tag{50}$$

$$v_\theta(0) = 0. \tag{51}$$

Using the Fortran Numerical Recipes implementation of the fourth-order Runge Kutta algorithm [42], the integrations are carried out with a time step of $\Delta t = 1$ s except near latitude extrema and pole crossings, where smaller time steps are used [28]. The time at which the puck returns to its initial latitude is the period τ of its motion, and its angular frequency follows from $\omega = 2\pi/\tau$ (solid trace). The puck's zonal drift during that time is given by $\Delta\phi = \phi(\tau) - \phi(0)$ (solid trace). Its latitude range $\Delta\theta = \theta_{\rm east} - \theta_{\rm west}$ (solid trace) is the difference between the puck's maximum latitude $\theta_{\rm east}$, where it travels east,

and its minimum latitude $\theta_{\rm west}$, where it travels west. Its midlatitude is given by the average of these latitudes,

$$\theta_0 = \frac{\theta_{\rm east} + \theta_{\rm west}}{2}. \tag{52}$$

This midlatitude is used to calculate ω, $\Delta\theta$, and $\Delta\phi$ from Eqs. (32), (46), and (47) (dashed traces in Fig. 8).

The numerical integrations and the small-amplitude approximations of Fig. 8 agree as $\varepsilon \to 0$. This agreement helps to validate both the integrations and the approximations. The upper limit $\varepsilon = 0.86$ shown in Fig. 8 yields $\theta_{\rm east} = 89.7°$, meaning that the puck just misses passing over or around the north pole. Thus, the range of values of ε in Fig. 8 represents the full range of values for nonpolar circles (region A in Fig. 3) for the initial conditions considered. The agreement between numerical and small-amplitude results is good over this entire range. This agreement justifies our definition of the reference angle as the midlatitude θ_0 and indicates that the second-order amplitude expansion of Eqs. (43) captures the basic physics of nonpolar circles.

VI. POLAR CIRCLES

In this section, we investigate small-amplitude polar circles. These occur on boundary CD of Fig. 3 near junction C, where ε is small and the puck makes small westward-drifting circles that pass through a pole.

We consider a puck launched southward from a pole, at initial latitude $\theta(0) = \pm\pi/2$, which implies $\mathcal{L} = 0$ by Eq. (11a). Since $\mathcal{L}$ is conserved, Eq. (11a) demands that

$$\dot\phi = -\Omega \tag{53}$$

throughout the motion. Thus, the longitude satisfies

$$\phi(t) = \phi_0 - \Omega t, \tag{54}$$

where $\phi_0 = \phi(0)$ is the initial longitude of the puck.

Substituting Eq. (53) into Eq. (11b) gives an equation of motion governing the latitude θ,

$$\varepsilon^2 = \cos^2\theta + \frac{\dot\theta^2}{\Omega^2}. \tag{55}$$

It is convenient to define a small polar angle δ by

$$\theta = \pm\left(\frac{\pi}{2} - \delta\right), \tag{56}$$

with the "+" sign pertaining to motion near the north pole and the "−" sign pertaining to motion near the south pole. Then Eq. (55) becomes

$$\varepsilon^2 = \sin^2\delta + \frac{\dot\delta^2}{\Omega^2}. \tag{57}$$

We seek solutions to Eq. (57) that satisfy the initial condition $\delta(0) = 0$, which places the puck initially at a pole. As will be seen below, these solutions feature both positive and negative values of δ. Positive values satisfying $0 < \delta < \pi$ correspond to the usual latitude range $-\pi/2 < \theta < \pi/2$, while negative values satisfying $-\pi < \delta < 0$ correspond to superpolar latitudes $\pi/2 < |\theta| < 3\pi/2$. Setting $\dot\delta = 0$ in Eq. (57) gives bounds on the allowed range of polar angles $-\delta_{\rm max} \le \delta \le \delta_{\rm max}$, where

$$\delta_{\rm max} = \sin^{-1}\varepsilon \tag{58}$$

is the maximum polar angle. This angle vanishes for small ε, implying that small-amplitude motion is confined to the vicinity of a pole, where $|\delta|$ is small. For small $|\delta|$, Eq. (57) gives

$$\varepsilon^2 = \delta^2 + \frac{\dot\delta^2}{\Omega^2}. \tag{59}$$

Its solution is

$$\delta(t) = \varepsilon\sin\Omega t, \tag{60}$$

where we have imposed the initial condition $\delta(0) = 0$. Applying Eqs. (12) and the foregoing yield a solution through first order in ε,

$$\phi(t) = \phi_0 - \Omega t \tag{61a}$$

$$\theta(t) = \pm\left(\frac{\pi}{2} - \varepsilon\sin\Omega t\right) \tag{61b}$$

$$v_\phi(t) = -a\Omega\varepsilon\sin\Omega t \tag{61c}$$

$$v_\theta(t) = \mp a\Omega\varepsilon\cos\Omega t. \tag{61d}$$

These first-order equations ignore the westward drift of polar circles and describe uniform circular motion with angular frequency $\omega = 2\Omega$, period $\tau = 2\pi/\omega = \pi/\Omega$, speed $v = a\Omega\varepsilon$, and radius $r = v/\omega$. The upper sign describes clockwise motion starting at the north pole ($\theta_0 = +\pi/2$) and the lower sign describes counterclockwise motion starting at the south pole ($\theta_0 = -\pi/2$).

Because the argument of the trigonometric functions in Eqs. (61) is Ωt, these equations might seem to describe uniform circular motion with angular frequency Ω. To explain why the angular frequency is $\omega = 2\Omega$ and the period is $\tau = 2\pi/\omega$, we consider the motion of a puck launched southward from the north pole along the longitude line $\phi = \phi_0$. The puck's latitude and longitude both decrease with time, so the puck deflects westward (to the right) as it moves south. At time $t = \tau/2$ and at longitude $\phi = \phi_0 - \pi/2$, the puck reaches its southernmost latitude of $\theta = \pi/2 - \varepsilon$, where it travels due west. Its longitude continues to decrease with time while its latitude increases, implying a northward deflection. As $t \to \tau$, the puck returns to the north pole along the longitude line $\phi = \phi_0 - \pi$, which is on the same great circle as the line $\phi = \phi_0$. Thus, in a time $t = \tau$, the puck returns to its initial position and velocity and completes one cycle of the motion. The velocity components of Eqs. (61c) and (61d) ensure that this cycle is a clockwise circle executed at constant speed $v = a\Omega\varepsilon$ and radius $r = v/\omega$.

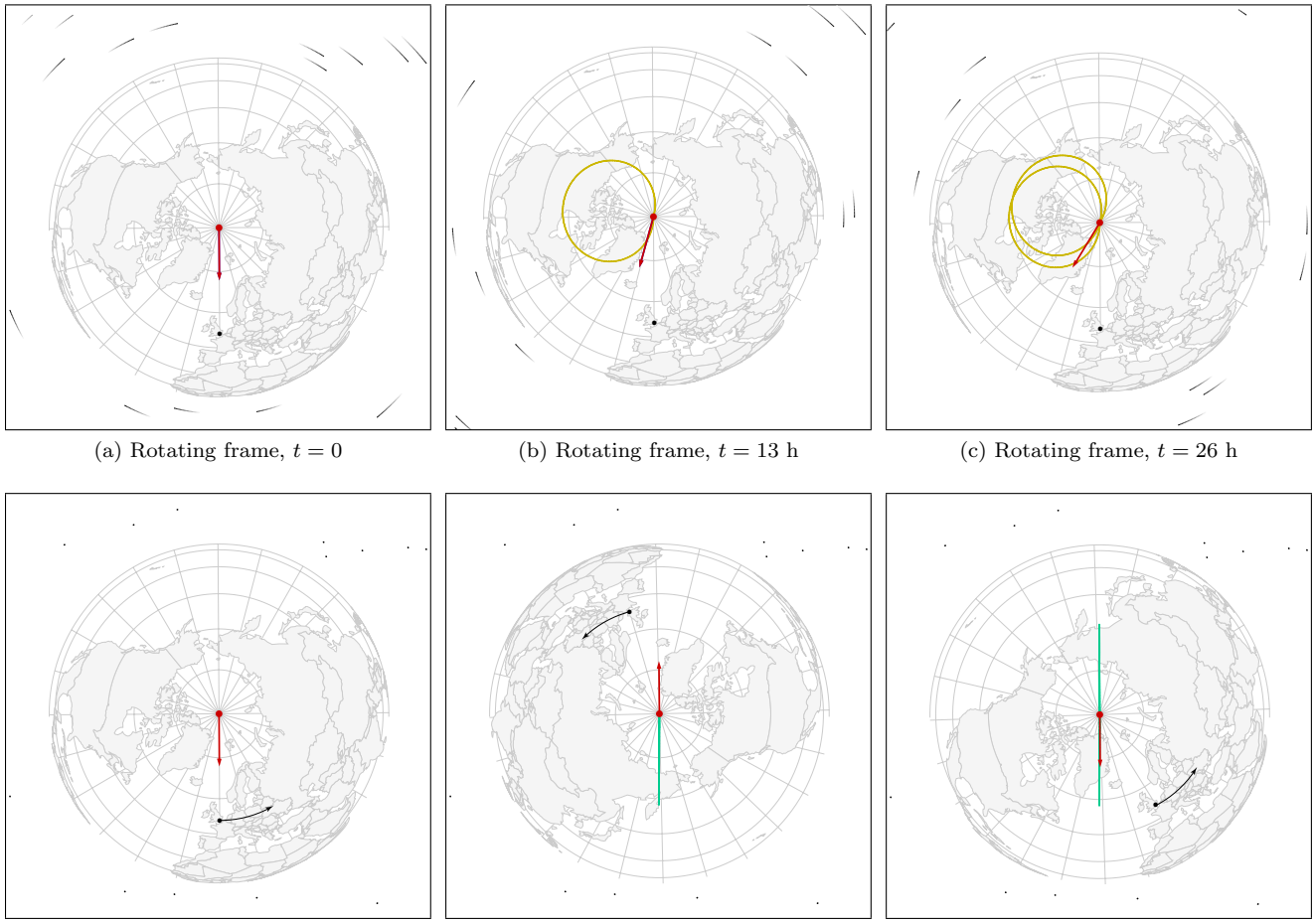

(a) Rotating frame, $t = 0$ (b) Rotating frame, $t = 13$ h (c) Rotating frame, $t = 26$ h

(d) Inertial frame, $t = 0$ (e) Inertial frame, $t = 13$ h (f) Inertial frame, $t = 26$ h

FIG. 9. *Corio Vis* screenshots of a puck launched from the north pole southward along the prime meridian at 250 m/s on a smooth, stably rotating, spheroidal earth, as seen by an observer above the north pole. Shown are screenshots at times $t = 0$, 13 h, and 26 h, as seen by observers in the rotating (a)-(c) and inertial (d)-(f) frames. The puck's position is denoted by a red dot and its velocity by a red arrow. The position of Greenwich, London, United Kingdom is denoted by a black dot and its velocity (due to the earth's rotation) is denoted by black arrows in the inertial frame. Yellow and green traces show the paths of the puck as seen by observers the rotating and inertial frames, respectively. In the rotating frame, the puck executes westward-drifting polar circles with period 13 h. In the inertial frame, the puck oscillates about the north pole with period 26 h. Background stars are denoted by black circular streaks in the rotating frame and by black dots in the inertial frame. *Corio Vis* demo 8 supplies views in both frames by using the mouse to rotate the viewing angle and by using the "f" key to toggle between reference frames [32].

The second cycle of motion described by Eqs. (61) is fascinating. Between times $t = \tau$ and $t = 2\tau$, the longitude decreases from $\phi = \phi_0 - \pi$ to $\phi = \phi_0 - 2\pi$, while the latitude $\theta > \pi/2$ is superpolar. Consequently, the puck resides on the opposite side of the north pole than is indicated by its longitude, and the puck traces out the same path as the first cycle. The transformations $\phi \to \phi + \pi$ and $\theta \to \pi - \theta$ map the values of ϕ and θ during the second cycle onto the values for the first cycle. Thereafter, odd-numbered cycles have latitudes in the usual range, while even-numbered cycles have superpolar latitudes and consequently replicate the motion of the odd-numbered cycles.

Figure 9 illustrates the motion of a puck launched southward from the north pole at 250 m/s ($\varepsilon = 0.54$), a typical cruising airspeed for commercial passenger aircraft [43]. As seen by an observer in the rotating frame (stationary earth, rotating stars), the puck executes polar circles with period $\tau = 13$ h and zonal drift $\Delta\phi = -16°$, meaning that it drifts westward by 16° during each period of its motion. This drift is evident in the velocity vectors in frames (b) and (c). As discussed above, odd-numbered cycles, such as the cycle between frames (a) and (b), have subpolar latitudes $\theta < \pi/2$ and even-numbered cycles, such as the cycle between frames (b) and (c), have superpolar latitudes $\theta > \pi/2$. These superpolar latitudes are evident in the numerical latitudes displayed in *Corio Vis*, demo 8 [32].

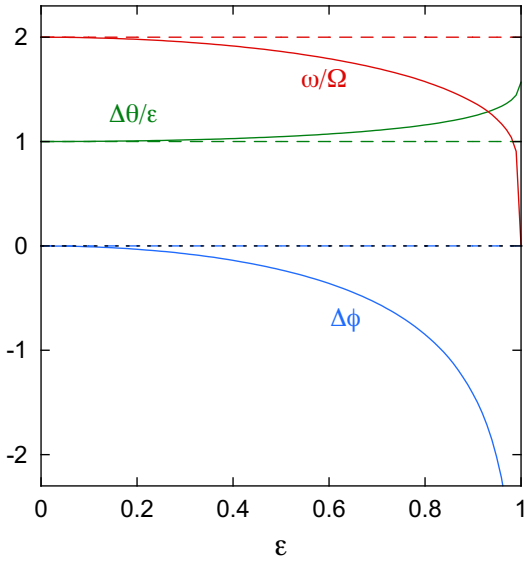

FIG. 10. Angular frequency ω, latitude range $\Delta\theta$ in radians, and zonal drift $\Delta\phi$ in radians vs. dimensionless speed ε for polar circles in the rotating frame, where Ω is the earth's angular speed of rotation. Solid traces are numerical solutions of Eqs. (11) and dashed traces are small-amplitude approximations given by Eqs. (62).

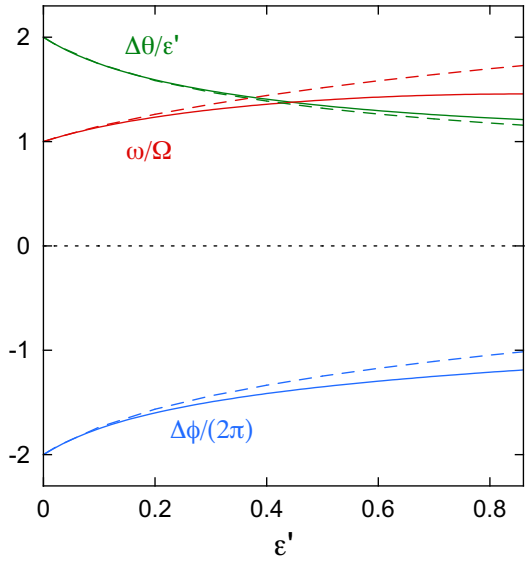

FIG. 11. Angular frequency ω, latitude range $\Delta\theta$ in radians, and zonal drift $\Delta\phi$ in radians vs. dimensionless speed ε' in the counter-rotating frame for circumpolar circles in the rotating frame, where Ω is the earth's angular speed of rotation. Solid traces are numerical solutions of Eqs. (11) and dashed traces are small-amplitude approximations given by Eqs. (63e), (64), and (65).

As seen by an observer in the inertial frame (rotating earth, stationary stars), the puck of Fig. 9 oscillates about the north pole, tracing out the same path again and again as the earth rotates beneath it. In this frame, the puck completes only half a cycle in time of 13 h and requires a time of 26 h to complete an entire oscillatory cycle. Thus, polar circles of period τ in the rotating frame correspond to polar oscillations of period 2τ in the inertial frame.

Equations (61) describe small-amplitude polar circles in the rotating frame with frequency, latitude range, and zonal drift given respectively by

$$\omega = 2\Omega \tag{62a}$$
$$\Delta\theta = \varepsilon \tag{62b}$$
$$\Delta\phi = 0, \tag{62c}$$

valid to first order in ε. Figure 10 compares these approximations with numerical solutions of Eqs. (11). The agreement is excellent for small ε.

VII. CIRCUMPOLAR CIRCLES

In this section, we investigate small-amplitude circumpolar circles. These occur in region A′ of Fig. 3 near the CE′ boundary, where ε' is small and the puck circles westward around a pole while making small excursions about a line of latitude. To describe these trajectories, we exploit the rotational/time-reversal symmetry of the earth (Secs. II B and III). Since Eqs. (43) satisfy Eqs. (11) to order ε^2, making the replacements $\phi \to \phi'$, $\mathcal{L} \to \mathcal{L}'$, and $\varepsilon \to \varepsilon'$ in Eqs. (43) satisfies Eqs. (18) to order ε'^2. Applying Eqs. (15) and (17b) immediately yields

$$\phi(t) = \phi_0 - 2\Omega t + \frac{\varepsilon'\Omega\sin\omega t}{\omega\cos\theta_0} + \frac{\varepsilon'^2\Omega t}{4\sin^2\theta_0} - \frac{\varepsilon'^2\Omega\sin 2\omega t}{2\omega\sin^2 2\theta_0}\left(1+\sin^2\theta_0\right) \tag{63a}$$
$$\theta(t) = \theta_0 - \frac{\varepsilon'\Omega}{\omega}\cos\omega t - \frac{\varepsilon'^2\Omega^2\sin^2\omega t}{\omega^2\sin 2\theta_0} \tag{63b}$$
$$\mathcal{L} = -\cos^2\theta_0 + \frac{\varepsilon'^2}{4\sin^2\theta_0}, \tag{63c}$$

where

$$\varepsilon'^2 = \varepsilon^2 + 4\mathcal{L} \tag{63d}$$
$$\omega = 2\Omega\sin\theta_0 \tag{63e}$$

from Eqs. (19) and (32). Equations (63) describe circumpolar circles with $\mathcal{L} < 0$ on the normally rotating earth to second order in the counter-rotating amplitude ε'. Like the nonpolar circles of Eqs. (43), these circumpolar circles run clockwise in the northern hemisphere ($\theta_0 > 0$, $\omega > 0$), and counterclockwise in the southern hemisphere ($\theta_0 < 0$, $\omega < 0$). Unlike the nonpolar circles of Eqs. (43), these circumpolar circles go around a pole and the puck always travels west, oscillating between latitudes $\theta_1 = \theta_0 - \varepsilon'\Omega/\omega$ (at times $t = 0,\ \tau,\ 2\tau, \ldots$, where

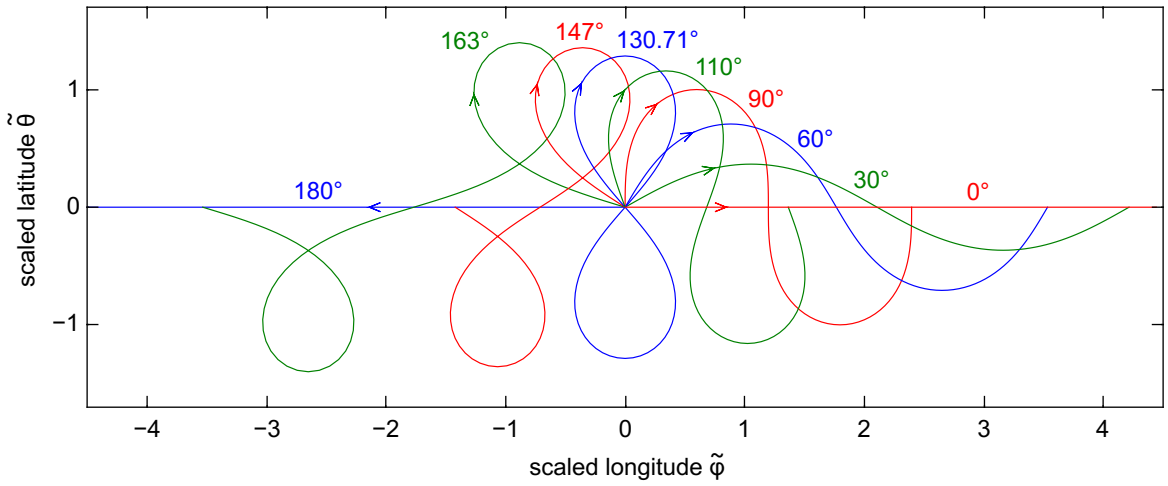

FIG. 12. Scaled puck trajectories for nonpolar waves obtained by integrating Eqs. (71a) and (71c). Shown are the scaled latitude $\tilde{\theta}$ vs. the scaled longitude $\tilde{\phi}$ for launches from the equator at various values of the launch angle α, measured north of east. A single period of the motion is shown for each value of α.

$\tau = 2\pi/|\omega|$ is the period) and $\theta_2 = \theta_0 + \varepsilon'\Omega/\omega$ (at times $t = \tau/2,\ 3\tau/2, \dots$). The latitude range is given by

$$\Delta\theta = |\theta_2 - \theta_1| = \frac{\varepsilon'}{|\sin\theta_0|}. \tag{64}$$

During one period τ of the motion, the puck migrates westward through a longitude range

$$\Delta\phi = \phi(\tau) - \phi(0) = -\frac{2\pi}{|\sin\theta_0|} + \frac{\pi\varepsilon'^2}{4|\sin^3\theta_0|}. \tag{65}$$

Setting $\varepsilon' = 0$ in Eq. (63d) gives $\mathcal{L} = -\varepsilon^2/4$, the angular momentum for westward motion at constant latitude θ_0 at a constant angular speed $\dot{\phi} = -2\Omega$ (boundary CE′ of Fig. 3). Such motion corresponds to stationary states on the counter-rotating earth.

To test the validity of Eqs. (63), we first observe that circumpolar circles in the rotating frame [Fig. 5(b)] correspond to nonpolar circles in the counter-rotating frame [Fig. 5(d)], with the puck traveling east when it is nearest the equator. For an eastward launch from latitude $\theta = \theta_1$ in this frame, Eq. (14b) allows us to relate the puck's dimensionless speed $(v)_{S'}$ in the counter-rotating frame to its initial eastward velocity component $v_\phi(0)$ in the normally rotating frame,

$$(v)_{S'} = 2\Omega a\cos\theta_1 + v_\phi(0), \tag{66}$$

where we have set $\rho = a\cos\theta_1$ in the weakly spheroidal approximation. Inserting this result into Eq. (17a) gives

$$v_\phi(0) = \Omega a\left(\varepsilon' - 2\cos\theta_1\right). \tag{67}$$

For small ε', $v_\phi(0) < 0$ and an eastward launch in the counter-rotating frame corresponds to westward launch in the normally rotating frame, with $v_\theta(0) = 0$.

Figure 11 compares the predictions of Eqs. (63e), (64), and (65) with numerical solutions of Eqs. (11) for westward launches at initial latitude $\theta_1 = 30°$ for various values of ε'. Equation (67) gives the initial westward velocity of the puck in the rotating frame. The maximum latitude θ_2 is found by integrating Eqs. (11) and the mid-latitude is determined by

$$\theta_0 = \frac{\theta_1 + \theta_2}{2}. \tag{68}$$

This value is used to determine the small-amplitude approximations for ω, $\Delta\theta$, and $\Delta\phi$ from Eqs. (63e), (64), and (65). Results for ω and $\Delta\theta$ in Fig. 11 are identical to those in Fig. 8 because the initial conditions for these figures were chosen to exploit the rotational/time-reversal symmetry of Fig. 5.

VIII. NONPOLAR WAVES

In this section, we investigate small-amplitude nonpolar waves, which occur in region B of Fig. 3 near junction E, where ε is small. The puck is stationary at the equator at junction E, so we can expect small-amplitude polar waves to move slowly near the equator. Because the Coriolis force vanishes at the equator, the amplitude expansion of Eqs. (22) fails for these waves and the wave frequency ω turns out to be proportional to $\sqrt{\varepsilon}$.

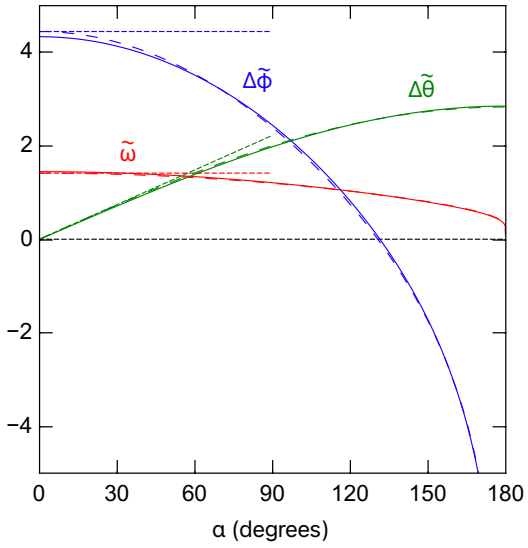

FIG. 13. Scaling results from Eqs. (71a) and (71c) (dashed traces) and exact results for $\varepsilon = 0.1$ from Eqs. (11) (solid traces) for the scaled frequency $\tilde{\omega}$, zonal drift $\Delta\tilde{\phi}$, and latitude range $\Delta\tilde{\theta}$ vs. the horizontal launch angle α for nonpolar waves. Dotted traces give the $\alpha \to 0$ limits of Eqs. (77b), (79), and (82) for eastward nonpolar waves.

The latitude θ is small for small-amplitude motion near the equator, and we assume $\dot{\theta}$ and $\dot{\phi}$ to be small as well. Employing the small-θ approximation $\cos^2\theta = 1 - \theta^2$ in Eqs. (11) and keeping the θ^2 contribution only where it does not multiply $\dot{\phi}$ yields

$$\frac{\dot{\phi}}{\Omega} = \mathcal{L} - 1 + \theta^2 \tag{69a}$$

$$\varepsilon^2 = \frac{\dot{\phi}^2}{\Omega^2} + \frac{\dot{\theta}^2}{\Omega^2}. \tag{69b}$$

It is convenient to define a scaled longitude $\tilde{\phi}(\tilde{t})$, a scaled latitude $\tilde{\theta}(\tilde{t})$, and a scaled dimensionless time $\tilde{t}$ by

$$\phi(t) = \sqrt{\varepsilon}\,\tilde{\phi}(\tilde{t}) \tag{70a}$$

$$\theta(t) = \sqrt{\varepsilon}\,\tilde{\theta}(\tilde{t}) \tag{70b}$$

$$\tilde{t} = \Omega\sqrt{\varepsilon}\,t. \tag{70c}$$

Inserting these definitions into Eqs. (69) yields scaled equations of motion

$$\frac{d\tilde{\phi}}{d\tilde{t}} = \cos\alpha + \tilde{\theta}^2 \tag{71a}$$

$$1 = \left(\frac{d\tilde{\phi}}{d\tilde{t}}\right)^2 + \left(\frac{d\tilde{\theta}}{d\tilde{t}}\right)^2, \tag{71b}$$

where Eq. (71a) ensures conservation of angular momentum in the inertial frame and Eq. (71b) ensures conservation of kinetic energy in the rotating frame. The square root of Eq. (71b) gives the net scaled dimensionless angular speed of the puck as it slides along the earth's frictionless surface. This speed is constant, and equals unity. Inserting Eq. (71a) into Eq. (71b) gives a convenient equation in $\tilde{\theta}$ only,

$$\frac{d\tilde{\theta}}{d\tilde{t}} = \pm\sqrt{1 - \left(\cos\alpha + \tilde{\theta}^2\right)^2}. \tag{71c}$$

In Eqs. (71), all dependencies on ε and $\mathcal{L}$ are subsumed into a dimensionless constant α defined by

$$\cos\alpha = \frac{\mathcal{L} - 1}{\varepsilon}. \tag{72}$$

Its range $0 \le \alpha \le \pi$ corresponds to the range $1 - \varepsilon < \mathcal{L} < 1 + \varepsilon$ of nonpolar waves (region B) of Fig. 3 for $\varepsilon < 1$. To interpret α, we consider equator crossings by setting $\tilde{\theta} = 0$ in Eqs. (71a) and (71c);

$$\frac{d\tilde{\phi}}{d\tilde{t}} = \cos\alpha \tag{73a}$$

$$\frac{d\tilde{\theta}}{d\tilde{t}} = \pm\sin\alpha. \tag{73b}$$

Here the "+" sign gives northward crossings and the "−" sign gives southward crossings. Adopting the "+" sign and dividing Eq. (73b) by Eq. (73a) gives

$$\frac{d\tilde{\theta}}{d\tilde{\phi}} = \tan\alpha. \tag{74}$$

The left side of this equation gives the slope of the trajectory at northward equator crossings, the ratio of the northward angular displacement $d\tilde{\theta}$ to the eastward angular displacement $d\tilde{\phi}$. Accordingly, α can now be interpreted as the angle of the puck's trajectory during northward equator crossings, measured north of east. At such crossings, the puck has an eastward velocity component for $0 \le \alpha < \pi/2$, has a westward velocity component for $\pi/2 < \alpha \le \pi$, and has a velocity that is directly northward for $\alpha = \pi/2$. Taking $\tilde{t} = 0$ at such crossings, α becomes the initial launch angle of the puck, measured north of east, for a horizontal launch at the equator.

Setting $d\tilde{\theta}/d\tilde{t} = 0$ and $\tilde{\theta} = \pm\tilde{\theta}^*$ in Eq. (71c) yields the scaled amplitude of the oscillations

$$\tilde{\theta}^* = \sqrt{2}\sin\frac{\alpha}{2}. \tag{75}$$

The puck oscillates between $\tilde{\theta} = +\tilde{\theta}^*$ (just north of the equator) and $\tilde{\theta} = -\tilde{\theta}^*$ (just south of the equator). Its scaled latitude range is

$$\Delta\tilde{\theta} = 2\tilde{\theta}^* = 2\sqrt{2}\sin\frac{\alpha}{2}. \tag{76}$$

We integrate Eqs. (71a) and (71c) using the fourth-order Runge-Kutta algorithm starting from the initial

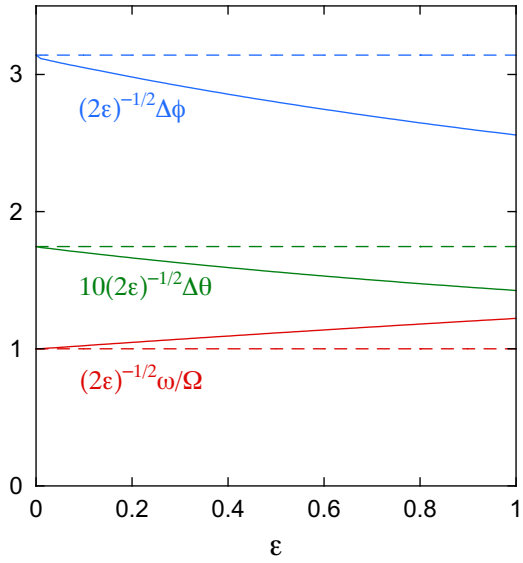

FIG. 14. Angular frequency ω, latitude range $\Delta\theta$ in radians, and zonal drift $\Delta\phi$ in radians vs. dimensionless speed ε for eastward nonpolar waves in the rotating frame for a launch angle of $\alpha = 10°$ north of east, where Ω is the earth's angular speed of rotation. Solid traces are numerical solutions of Eqs. (11) and dashed traces are small-amplitude approximations given by Eqs. (84).

northward equator crossing at $\tilde{t} = 0$. Shown in Fig. 12 are resulting trajectories for various values of α. For $\alpha = 130.71°$, the trajectory is a figure eight that closes on itself. For $\alpha < 130.71°$, the puck drifts eastward, and for $\alpha > 130.71°$, the puck drifts westward.

The time $\tilde{t}$ of the second northward equator crossing (after the initial northward crossing at $\tilde{t} = 0$) is the scaled period $\tilde{\tau}$ of the motion, obtained by integrating Eqs. (71a) and (71c). Shown as dashed traces in Fig. 13 are the scaled angular frequency $\tilde{\omega} = 2\pi/\tilde{\tau}$, the scaled latitude range of Eq. (76), and the scaled zonal drift $\Delta\tilde{\phi} = \tilde{\phi}(\tilde{\tau}) - \tilde{\phi}(0)$ obtained by integrating Eqs. (71a) and (71c), as functions of α. Shown as solid traces in Fig. 13 are exact numerical results for $\varepsilon = 0.1$ obtained by integrating Eqs. (11). The exact and scaling results agree to within 3% over the range $0 \le \alpha \le 180°$.

A. Eastward Nonpolar Waves

It is instructive to consider small-amplitude nonpolar waves with small α, which are described by simple eastward sinusoidal motion. In Fig. 3, this motion occurs in region B (nonpolar waves), near junction E (stationary at equator), and near boundary EF (eastward at equator).

To lowest order in α and $\tilde{\theta}$, Eqs. (71c), (75), and (76) give

$$\frac{d\tilde{\theta}}{d\tilde{t}} = \pm\sqrt{\alpha^2 - 2\tilde{\theta}^2} \tag{77a}$$

$$\tilde{\theta}^* = \frac{\alpha}{\sqrt{2}} \tag{77b}$$

$$\Delta\tilde{\theta} = 2\tilde{\theta}^* = \sqrt{2}\alpha. \tag{77c}$$

The solution

$$\tilde{\theta}(\tilde{t}) = \tilde{\theta}^* \sin(\tilde{\omega}\tilde{t}) \tag{78}$$

satisfies the initial condition $\tilde{\theta}(0) = 0$, where

$$\tilde{\omega} = \sqrt{2} \tag{79}$$

is the dimensionless angular frequency and

$$\tilde{\tau} = \frac{2\pi}{\tilde{\omega}} = \sqrt{2}\pi \tag{80}$$

is the scaled period. Because Eq. (71a) gives $d\tilde{\phi}/d\tilde{t} = 1$ to lowest order, demanding $\tilde{\phi}(0) = 0$ gives

$$\tilde{\phi}(\tilde{t}) = \tilde{t} \tag{81}$$

and

$$\Delta\tilde{\phi} = \tilde{\tau} = \sqrt{2}\pi. \tag{82}$$

In summary, small-amplitude eastward nonpolar waves have the sinusoidal form

$$\phi(t) = \Omega\varepsilon t \tag{83a}$$

$$\theta(t) = \alpha\sqrt{\frac{\varepsilon}{2}}\sin(\omega t), \tag{83b}$$

with angular frequency

$$\omega = \sqrt{2\varepsilon}\,\Omega, \tag{84a}$$

latitude range

$$\Delta\theta = \sqrt{2\varepsilon}\alpha, \tag{84b}$$

and (eastward) zonal drift

$$\Delta\phi = \sqrt{2\varepsilon}\pi. \tag{84c}$$

Evidently, the frequency ω of these oscillations vanishes with vanishing amplitude ε.

Given values of the dimensionless speed ε and the launch angle α, the puck's constant speed $(v)_S = \varepsilon\Omega a$ follows from Eq. (9a) and the initial velocity becomes

$$(\mathbf{v})_S(0) = \varepsilon\Omega a\left(\cos\alpha\,\hat{\phi} + \sin\alpha\,\hat{\theta}\right). \tag{85}$$

Setting this equal to Eq. (2) gives the initial velocity components in the rotating frame,

$$v_\phi(0) = \varepsilon\Omega a\cos\alpha \tag{86}$$

$$v_\theta(0) = \varepsilon\Omega a\sin\alpha. \tag{87}$$

Figure 14 compares the small-amplitude approximations of Eqs. (84) (dashed traces) with numerical solutions of Eqs. (11) (solid traces) as a function of ε, for $\alpha = 10°$. The small-amplitude approximations converge to the exact results as $\varepsilon \to 0$.

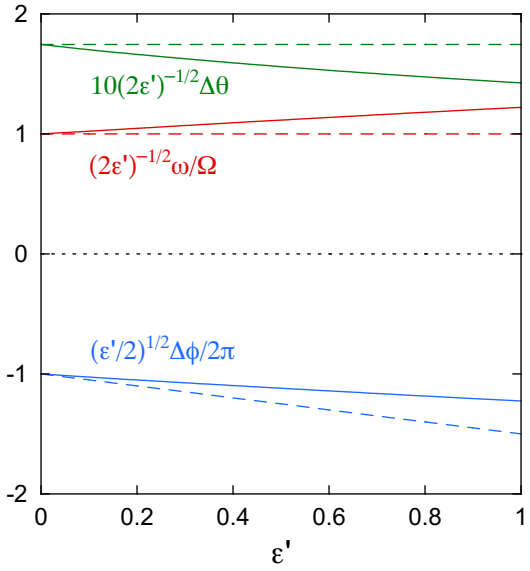

FIG. 15. Angular frequency ω, latitude range $\Delta\theta$ in radians, and zonal drift $\Delta\phi$ in radians vs. counter-rotating dimensionless speed ε' for westward circumpolar waves in the rotating frame for a launch angle of $\alpha = 10^\circ$ north of west in the counter-rotating frame, where Ω is the earth's angular speed of rotation. Solid traces are numerical solutions of Eqs. (11) and dashed traces are small-amplitude approximations given by Eqs. (90).

IX. WESTWARD CIRCUMPOLAR WAVES

In this section, we investigate small-amplitude westward circumpolar waves that occur in region B′ of Fig. 3, near junction E′ and boundary E′F′. These waves circle around both poles and remain close to the equator, traveling westward. To describe these waves, we exploit the rotational/time-reversal symmetry of the earth (Secs. II B and III) to transform eastward nonpolar waves in the rotating frame (Sec. VIII A), with the equatorial launch angle α measured north of east, into westward nonpolar waves in the counter-rotating frame, with α measured north of west. When viewed in the rotating frame, these become westward circumpolar waves.

Making the replacements $\phi \to \phi'$, $\mathcal{L} \to \mathcal{L}'$, and $\varepsilon \to \varepsilon'$ in Eqs. (83) and applying Eqs. (15) and (17b) yields

$$\phi(t) = -\Omega\,(2+\varepsilon')\,t \tag{88a}$$

$$\theta(t) = \alpha\sqrt{\frac{\varepsilon'}{2}}\,\sin(\omega t), \tag{88b}$$

where

$$\varepsilon'^2 = \varepsilon^2 + 4\mathcal{L} \tag{89}$$

is the counter-rotating amplitude,

$$\omega = \sqrt{2\varepsilon'}\,\Omega \tag{90a}$$

is the angular frequency,

$$\Delta\theta = \sqrt{2\varepsilon'}\alpha, \tag{90b}$$

is the latitude range, and

$$\Delta\phi = -\sqrt{\frac{2}{\varepsilon'}}\pi\,(2+\varepsilon')\,. \tag{90c}$$

is the (westward) zonal drift. This drift becomes unbounded as $\varepsilon' \to 0$, reflecting the unbounded period of motion in this limit.

For a launch from the equator at an angle α measured north of west in the counter-rotating frame, the initial velocity in this frame is given by

$$(\mathbf{v})_{S'}(0) = \varepsilon'\Omega a\left(-\cos\alpha\,\hat{\phi} + \sin\alpha\,\hat{\theta}\right), \tag{91}$$

where Eq. (17a) gives the puck's constant speed $(v)_{S'} = \varepsilon'\Omega a$. Setting Eq. (91) equal to Eq. (14b) and setting $\rho = a$ for an equatorial launch in the weakly spheroidal approximation gives the corresponding components of the initial velocity in the normally rotating frame

$$v_\phi(0) = -\Omega a\,(2+\varepsilon'\cos\alpha) \tag{92a}$$

$$v_\theta(0) = \varepsilon'\Omega a\sin\alpha. \tag{92b}$$

Figure 15 compares the predictions of Eqs. (90) with numerical solutions of Eqs. (11) with this initial velocity, with initial position $\theta(0) = \phi(0) = 0$, and with $\alpha = 10^\circ$, as a function of ε'. Results for ω and $\Delta\theta$ in Fig. 15 are identical to those in Fig. 14 because the initial conditions for these figures were chosen to exploit the rotational/time-reversal symmetry.

X. CONCLUSIONS

We have identified, named, and described sixteen classes of trajectories that are possible for motion on the surface of a frictionless spheroidal earth. We have exploited our *CorioVis* visualization software [32] and the earth's rotational/time-reversal symmetry to develop and validate small-amplitude descriptions for the four main classes and one degenerate class. These efforts illuminate the rich variety of motions that are possible on the earth's surface.

Small-amplitude nonpolar circles have been observed in ocean currents [8, 33–38]. It would be interesting to see if other classes might be observable in ocean or atmospheric currents. Of particular interest are nonpolar waves, which might be observable in ocean currents near the equator. This is a challenging observation, though, because small-amplitude nonpolar waves have low frequencies and might therefore be overwhelmed by other oceanic forces such as pressure gradients, mean currents, or continental or bottom barriers.

XI. ACKNOWLEDGMENTS

We gratefully acknowledge helpful discussions with Jared Arnell, Nathan Edwards, Anders Persson, and Hillary Swanson, and support from U.S. NSF grant No. 1808225.

[1] Joseph M Moran. *Weather studies: Introduction to atmospheric science*. American Meteorological Society, Boston, Massachusetts, 5th edition, 2012.

[2] David Thomas and David George Bowers. *Introducing Oceanography*. Dunedin Academic Press Ltd, 2012.

[3] Owen E Thompson. Coriolis deflection of a ballistic projectile. *American Journal of Physics*, 40(10):1477–1483, 1972.

[4] Nicholas Brewster, Tendayi Kerr, Nathan Adams, and Jason Smith. P4_5 bending bullets. *Physics Special Topics*, 10(1), 2011.

[5] Miguel Ángel Sánchez-Tena, Cristina Alvarez-Peregrina, M^{a} Carolina Valbuena-Iglesias, and Pablo Ruisoto Palomera. Optical illusions and spatial disorientation in aviation pilots. *Journal of medical systems*, 42(5):1–5, 2018.

[6] R Haviland. Influence of Coriolis forces on some design choices in rotating spacecraft. In *Weightlessness and Artificial Gravity Meeting*, page 889, 1997.

[7] National Geographic. Coriolis Effect Demonstration. `https://youtu.be/mPsLanVS1Q8` (accessed 21-Nov-2018), 2018.

[8] A Persson. The Coriolis effect: Four centuries of conflict between common sense and mathematics, Part I: A history to 1885. *History of Meteorology*, 2:1–24, 2005.

[9] Gaspard Gustave Coriolis. Mémoire sur les équations du mouvement relatif des systèmes de corps. *J. Ecole Polytech.*, 15:142–54, 1835.

[10] Norman A Phillips. An explication of the Coriolis effect. *Bulletin of the American Meteorological Society*, 81(2):299–304, 2000.

[11] John R Taylor. *Classical Mechanics*. University Science Books, 2005.

[12] Steven Ackerman and John Knox. *Meteorology*. Jones & Bartlett Publishers, 2015.

[13] David H McIntyre. Using great circles to understand motion on a rotating sphere. *American Journal of Physics*, 68(12):1097–1105, 2000.

[14] R Stacey and P Davis. *Physics of the Earth*. Cambridge University Press, 2008.

[15] Anders Persson. How do we understand the Coriolis force? *Bulletin of the American Meteorological Society*, 79(7):1373–1386, 1998.

[16] Boyd Edwards and John Edwards. Forces and conservation laws for motion on our spheroidal Earth. *American Journal of Physics*, 89:830–842, 2021.

[17] Benoit Cushman-Roisin. Motion of a free particle on a beta-plane. *Geophysical & Astrophysical Fluid Dynamics*, 22(1-2):85–102, 1982.

[18] Jeffrey J Early. The forces of inertial oscillations. *Quarterly Journal of the Royal Meteorological Society*, 138(668):1914–1922, 2012.

[19] P Ripa. "Inertial" oscillations and the β-plane approximation(s). *Journal of Physical Oceanography*, 27(5):633–647, 1997.

[20] P Ripa. Effects of the earth's curvature on the dynamics of isolated objects. Part I: The disk. *Journal of Physical Oceanography*, 30(8):2072–2087, 2000.

[21] P Ripa. Effects of the earth's curvature on the dynamics of isolated objects. Part II: The uniformly translating vortex. *Journal of Physical Oceanography*, 30(10):2504–2514, 2000.

[22] Nathan Paldor and Peter D Killworth. Inertial trajectories on a rotating earth. *Journal of the Atmospheric Sciences*, 45(24):4013–4019, 1988.

[23] Nathan Paldor and Andrey Sigalov. The mechanics of inertial motion on the earth and on a rotating sphere. *Physica D: Nonlinear Phenomena*, 160(1-2):29–53, 2001.

[24] Nathan Paldor. The zonal drift associated with time-dependent particle motion on the earth. *Quarterly Journal of the Royal Meteorological Society*, 127(577):2435–2450, 2001.

[25] Nathan Paldor. Inertial particle dynamics on the rotating earth. In A Griffa, AD Kirwan, AJ Mariano, T Özgökmen, and T Rossby, editors, *Lagrangian Analysis and Prediction of Coastal and Ocean Dynamics*, chapter 5, pages 119–135. Cambridge University Press, Cambridge, 2007.

[26] FJW Whipple. XLIV. The motion of a particle on the surface of a smooth rotating globe. *The London, Edinburgh, and Dublin Philosophical Magazine and Journal of Science*, 33(198):457–471, 1917.

[27] Stephen A Pennell and Keith L Seitter. On inertial motion on a rotating sphere. *Journal of the Atmospheric Sciences*, 47(16):2032–2034, 1990.

[28] Boyd Edwards and John Edwards. Geodetic model for teaching motion on the Earth's spheroidal surface. *European Journal of Physics*, 43:015003 (20 pp), 2022.

[29] Helmut Moritz. Geodetic reference system 1980. *Journal of Geodesy*, 74(1):128–133, 2000.

[30] Wikipedia. World Geodetic System. `https://en.wikipedia.org/wiki/World_Geodetic_System#WGS84` (accessed 03-18-2021), 2021.

[31] Bernhard Hofmann-Wellenhof, Herbert Lichtenegger, and James Collins. *Global positioning system: theory and practice*. Springer-Verlag, 1994.

[32] John M. Edwards and Boyd F. Edwards. *CorioVis* Coriolis Visualization Software. `https://edwardsjohnmartin.github.io/coriolis/` (accessed 26-July-2020), 2020.

[33] Dale R Durran. Is the Coriolis force really responsible for the inertial oscillation? *Bulletin of the American Meteorological Society*, 74(11):2179–2184, 1993.

[34] Anders Persson. Is the Coriolis effect an 'optical illusion'? *Quarterly Journal of the Royal Meteorological Society*, 141(690):1957–1967, 2015.

[35] James R Holton and Gregory J Hakim. *An Introduction to Dynamic Meteorology*, volume 88. Academic Press, 2013.

[36] Federico Graef. On the westward translation of isolated eddies. *Journal of Physical Oceanography*, 28(4):740–745, 1998.

[37] GA Jacobs, JW Book, HT Perkins, and WJ Teague. Inertial oscillations in the Korea Strait. *Journal of Geophysical Research: Oceans*, 106(C11):26943–26957, 2001.

[38] Thomas WN Haine and Deepak A Cherian. Analogies of ocean/atmosphere rotating fluid dynamics with gyroscopes: Teaching opportunities. *Bulletin of the American Meteorological Society*, 94(5):673–684, 2013.

[39] W James Steenburgh, David M Schultz, and Brian A Colle. The structure and evolution of gap outflow over the Gulf of Tehuantepec, Mexico. *Monthly Weather Review*, 126(10):2673–2691, 1998.

[40] Aksel C Wiin-Nielsen. On inertial flow on the sphere: Technical report. Technical report, 1973.

[41] Adrian E Gill. *Atmosphere-Ocean Dynamics*. Academic press, 1982.

[42] William H Press, Saul A Teukolsky, William T Vetterling, and Brian P Flannery. *Numerical Recipes in Fortran 90: Numerical recipes in Fortran 77V. 2. Numerical recipes in Fortran 90*. Cambridge University Press, 1996.

[43] Wikipedia. Cruise (aeronautics). `https://en.wikipedia.org/wiki/Cruise_(aeronautics)` (accessed 03-18-2021), 2021.